Contrib Mineral Petrol (2006) 151: 245–266
DOI 10.1007/s00410-006-0065-8

ORIGINAL PAPER

Cristina Perinelli · Pietro Armienti · Luigi Dallai

Geochemical and O-isotope constraints on the evolution of lithospheric mantle in the Ross Sea rift area (Antarctica)

Received: 8 August 2005 / Accepted: 11 January 2006 / Published online: 9 February 2006

Abstract Peridotite xenoliths found in Cenozoic alkali basalts of northern Victoria Land, Antarctica, vary from fertile spinel-lherzolite to harzburgite. They often contain glass-bearing pockets formed after primary pyroxenes and spinel. Few samples are composite and consist of depleted spinel lherzolite crosscut by amphibole veins and/or lherzolite in contact with poikilitic wehrlite. Peridotite xenoliths are characterized by negative Al_2O_3–Mg# and TiO_2–Mg# covariations of clino- and orthopyroxenes, low to intermediate HREE concentrations in clinopyroxene, negative Cr–Al trend in spinel, suggesting variable degrees of partial melting. Metasomatic overprint is evidenced by trace element enrichment in clinopyroxene and sporadic increase of Ti–Fe_{tot}. Preferential Nb, Zr, Sr enrichments in clinopyroxene associated with high Ti–Fe_{tot} contents constrain the metasomatic agent to be an alkaline basic melt. In composite xenoliths, clinopyroxene REE contents increase next to the veins suggesting metasomatic diffusion of incompatible element. Oxygen isotope data indicate disequilibrium conditions among clinopyroxene, olivine and orthopyroxene. The highest $\delta^{18}O$ values are observed in minerals of the amphibole-bearing xenolith. The $\delta^{18}O_{cpx}$ correlations with clinopyroxene modal abundance and geochemical parameters (e.g. Mg# and Cr#) suggest a possible influence of partial melting on oxygen isotope composition. Thermobarometric estimates define a geotherm of 80°C/GPa for the refractory lithosphere of NVL, in a pressure range between 1 and 2.5 GPa. Clinopyroxene microlites of melt pockets provide P–T data close to the anhydrous peridotite solidus and confirm that they originated from heating and decompression during transport in the host magma. All these geothermometric data constrain the mantle potential temperature to values of 1250–1350°C, consistent with the occurrence of mantle decompressional melting in a transtensive tectonic regime for the Ross Sea region.

Keywords Metasomatism · Lithospheric mantle · Mantle geotherm · Ross Sea Rift · Antarctica

Communicated by J. Hoefs

C. Perinelli (✉) · P. Armienti
Dipartimento di Scienze della Terra, Universitá degli Studi di Pisa, Via S. Maria 53, 56126 Pisa, Italy
E-mail: cperinelli@dst.unipi.it
Tel.: +39-50-2215708
Fax: +39-50-2215800
E-mail: armienti@dst.unipi.it

L. Dallai
IGG – CNR, Via Moruzzi 1, 56124 Pisa, Italy
E-mail: dallai@igg.cnr.it

Introduction

Spinel peridotite xenoliths found in alkali basalts provide evidence for the composition of lithospheric mantle and constrain the nature, evolution and thermal state of the uppermost mantle in regions of continental rift.

Ultramafic nodules are abundant in basic lavas of the McMurdo Volcanic Group (MMVG), in the Ross Sea region of Antarctica, an area of ongoing rifting where magmatism has been active since Cenozoic times. A general consensus for the origin of this magmatism has not yet been achieved. The main hypotheses proposed can be summarized as follows: (1) active rifting due to the presence of a thermally buoyant plume; (2) passive rifting related to transtensional tectonics and consequent melting of the low-melting domains in the lithospheric mantle. The latter hypothesis included the possibility that partial melting preferentially sampled a fossil HIMU plume emplaced during Gondwana break-up (LeMasurier and Rex 1989; Thessenson and Wörner 1991; Kyle et al. 1992; Rocholl et al. 1995; LeMasurier and Landis 1996; Hart et al. 1997; Wörner 1999; Storti et al. 2001; Rocchi et al. 2002).

Previous studies have shown that the mantle in this area is heterogeneous and that mantle xenoliths preserved evidence for partial melting and metasomatic processes (Berg et al. 1989; Hornig and Wörner 1991; Beccaluva et al. 1991; Hornig et al. 1992; Zipfel and

Wörner 1992; Coltorti et al. 2004). According to Zipfel and Wörner (1992), the mantle xenoliths record three main stages: (1) adiabatic rise and dynamic high-temperature recrystallization of mantle phases at lower pressure; (2) cooling and re-crystallization under low pressure; (3) local heating of lithospheric mantle linked to the magmatism of Ross Sea Rift. During this late stage and before xenoliths were brought to surface, metasomatic processes affected lithospheric mantle domains of this region likely due to the infiltration of basaltic melts at depth (Coltorti et al. 2004).

In this study we investigated two suites of spinel peridotites for major element, trace element and O-isotope composition in order to constrain their petrologic evolution and to define the thermal state of the lithosphere. Combining the REE distribution with oxygen isotope data, we constrained the processes of partial melting and metasomatism affecting the lithospheric mantle during the Cenozoic.

Geological setting

The MMVG igneous activity is linked to the West Antarctic Rift System (WARS, Tessensohn and Wörner 1991), a region of lithospheric thinning marked by a topographical trough from the Antarctic Peninsula to the Ross Embayment-northern Victoria Land (Fig. 1) (Behrendt et al. 1991, 1992; LeMasurier and Thomson 1990). The western rift flank in northern Victoria Land (NVL) is formed by the Transantarctic Mountains and represents the uplifted roots of the early Palaeozoic Ross Orogen. The uplift of the Transantarctic Mountains was substantially amagmatic and it was accompanied by extensional tectonics in the Ross Sea region during late Cretaceous time (e.g. Chand et al. 2001; Fitzgerald 1994; Fitzgerald and Stump 1997; Stagg and Willcox 1992).

Since the Eocene, diffuse igneous activity has characterized the WARS. In northern Victoria Land, plutons, like swarms and volcanoes were emplaced in an area of about 400×80 km (Fitzgerald and Stump 1997; Rocchi et al. 2002; Tonarini et al. 1997). The volcanic products were grouped in the McMurdo Volcanic Group (Kyle 1990), while intrusive-subvolcanic varieties are collectively referred to as Meander Intrusive Group (Muller et al. 1991; Tonarini et al. 1997). Mantle xenoliths were brought to surface by the primitive alkaline magmas (melanephelinite, basanite and alkali olivine basalt). These magmas erupted from monogenetic cinder

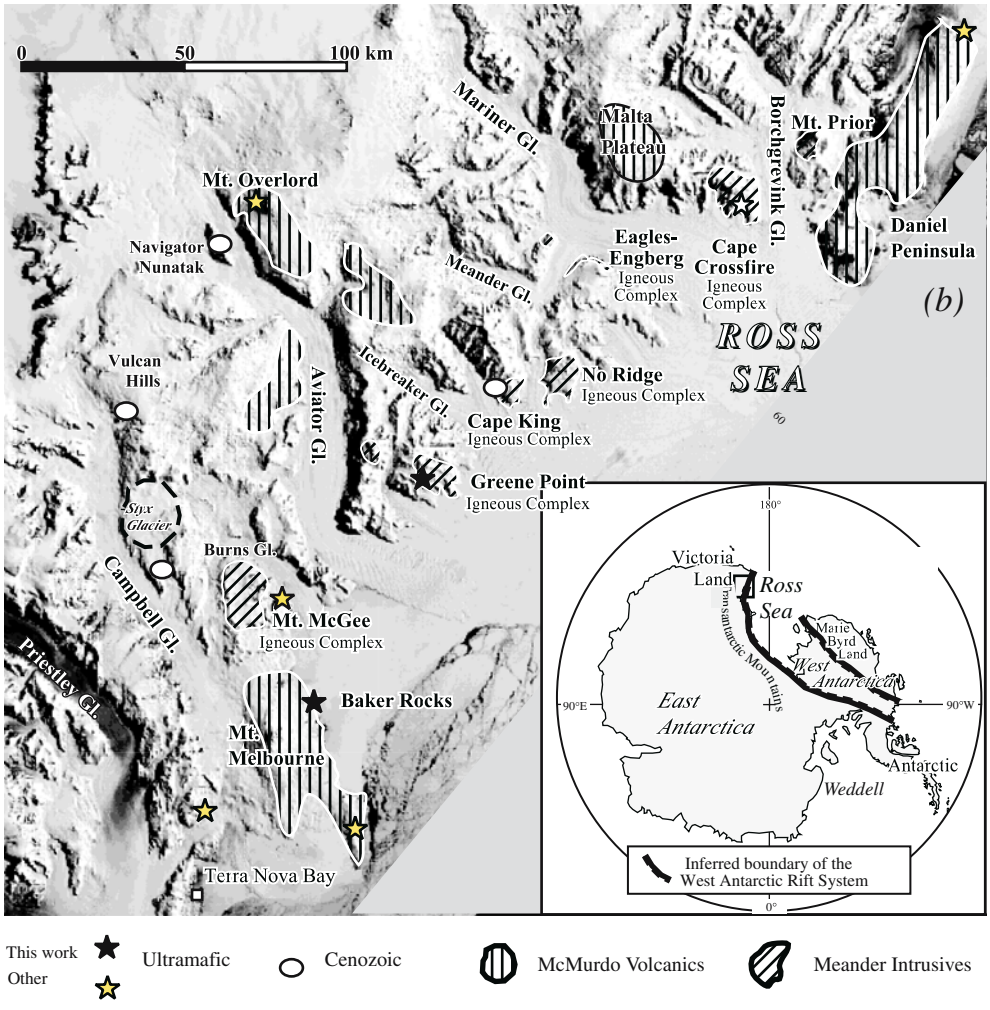

Fig. 1 Sketch map of north Victoria Land and sampling localities

cones near the margin of larger volcanoes or scattered on the crystalline basement, where the major active faults likely provided direct pathways for ascending to surface (Salvini et al. 1997; Orlando et al. 1997).

Analytical methods

The major elements of the whole rock were determined on powder pellets by XRF (Philips PW 1480) with the Franzini et al. (1975) correction, while trace elements were determined for selected samples by ICP-MS (Fisons PQ2 Plus®) at "Dipartimento di Scienze della Terra", Pisa University. Samples were dissolved in screw-top PFA vessels on a hotplate at ~120°C with HF-HNO3 mixture. Analyses were performed by external calibration using basaltic geochemical reference samples as composition- and matrix-matching calibration solutions. The correction procedure includes (i) blank subtraction; (ii) instrumental drift correction using Rh-Re-Bi internal standardization and repeated (every five samples) analysis of a drift monitor; (iii) oxide-hydroxide interference correction. Precision, evaluated by replicate dissolutions and analyses of the in-house standard HE-1 (Mt. Etna hawaiite), is generally between 2 and 5% RSD, except for Gd (6%), Tm (7%), Pb and Sc (8%). Detection limits are in the range 0.002–0.02 ng ml^{-1} in the solution (corresponding to 0.002–0.02 ppm for a 1,000-fold sample dilution) for all the elements, except for Ba, Pb and Sr $(0.1 \div 0.2)$.

The major elements of mineral and glass were analysed by CAMECA electron microprobe (Instituto di Geoscienze e Georisorse, Rome Section, Italy) operated at 15 kV accelerating voltage and 30 nA beam current. Counting time was 100 s. To reduce alkali loss during glass analysis, we decreased the counting time to 20 s and the beam was defocused to 15 μm. ZAF correction was applied to all data.

The concentration of trace elements in minerals of GP xenoliths were determined by laser ablation microprobe-inductively coupled plasma- mass spectrometry analysis (LAM-ICP-MS) at CNR- Istituto di Geoscienze e Georisorse in Pavia, Italy (operating conditions, analytical procedures, accuracy and precision have been described by Bottazzi et al. 1994).

Trace elements in minerals and intergranular glasses were determined by secondary ion mass spectrometry (SIMS) on polished sections at the LAM-ICP-MS laboratory of Pavia. Analytical procedures have been described by Wulff-Pedersen et al. (1999).

Oxygen isotope data were measured by conventional laser fluorination (Sharp 1995) at the CNR-Istituto di Geologia Ambientale e Geoingegneria in Rome, Italy. A 15 W CO_2 laser was employed to irradiate the samples and pure fluorine desorbed at 290–310°C from hexafluoropotassium–nickelate salt (Asprey 1976) was used to react 1–1.5 mg of cpx, opx, spl and ol fragments. The O_2 produced was purified of excess fluorine by a KBr trap at 160°C and of trace NF_x by-products of laser fluorination using a 13 Å zeolite molecular sieve and liquid nitrogen–ethanol mixture (Clayton and Mayeda 1983). The gas was then introduced into a Finnigan delta plus mass spectrometer and analyzed for oxygen isotope composition and mineral yields were controlled to be quantitative by an empirical regression curve based on samples with known $\delta^{18}O$ versus P_{O2} values in the MS bellow. A total of 23 NBS28 ($\delta^{18}O = 9.60‰$) standard samples were measured during the time of this study, with an average $\delta^{18}O$ value of $9.54 \pm 0.17‰$ (2σ). During each set of analyses, four to seven aliquots of laboratory quartz standards were measured with an average reproducibility of $\pm 0.10‰$ (1σ) and no data correction was adopted. All the results are reported in the standard per mil notation and the $\delta^{18}O$ values are relative to SMOW. At least two fragments were analyzed for each mineral and variation within the same sample is less than the precision of standards.

Samples

Spinel peridotite xenoliths were collected at Greene Point and Baker Rocks (Fig. 1). They show variable dimensions ranging from 3 to 10 cm. Modal compositions of larger nodules (> 5 cm) were estimated by counting more than 1,500 points in each thin section (Table 1). Xenoliths show a continuous mineralogical variation from moderately depleted lherzolite (11 to 12% diopside) to harzburgite with 0–4% of diopside (Table 1).

The most common texture is coarse-grained protogranular, but porphyroclastic and equigranular varieties also occur. Olivines and orthopyroxenes of protogranular samples are equant and show curvilinear grain boundaries. The maximum size reached is about 1 cm; typically, olivine crystal size shows a scale invariant distribution due to brittle fracturing (Armienti and Tarquini 2002). Clinopyroxene occurs both as a primary phase (CpxI) and microlites in pyrometamorphic glass patches (CpxII). Cpx I size is related to the depletion degree of the whole rock, the larger grains (up to 2 mm) occurring in the more fertile samples (modal clinopyroxene% > 6, Table 1). Coarse-grained orthopyroxene displays exsolution lamellae of clinopyroxene.

Spinel is commonly found next to diopside, sometimes showing symplectitic intergrowths with enstatite crystals. Reaction textures of spinel consist of colourless glass, neoblastic clinopyroxene and olivine. In porphyroclastic xenoliths, "holly leaf" spinel occurs in re-crystallized areas and defines a foliation.

A few samples have pyrometamorphic textures with spongy pyroxenes and grain rims replaced by a reaction assemblage of clinoproxene + olivine + glass. There is no evidence of direct connection between glass blebs and host lava due to the lack of veinlets of host magma in the xenoliths.

Table 1 Modes for xenoliths from Greene Point and Baker Rocks

	Sample	Rock	Ol	Opx	Cpx	Sp	Amph
	BR-213	Lh	69.6	22.5	7.3	0.6	
Composite	BR-214	Weh	73.9	4.6	20.9	0.6	
	BR-214	Lh	68.4	24.3	6.7	0.6	
Composite	BR-218	Lh	71.9	19.2	8.9	0.2	
	BR-218	Pargasite vein					100.0
Composite	BR-219	Weh	61.0	4.4	34.3	0.3	
	BR-219	Hz	80.7	15.5	3.6	0.2	
	GP1	Hz-Lh	70.4	23.3	5.1	1.2	
	GP5	Hz	74.5	18.7	4.9	1.9	
	GP6	Hz	76.5	18.2	4.2	1.2	
	GP10	Hz	75.4	17.3	5.4	1.9	
	GP14	Lh	66.2	20.5	11.9	1.4	
	GP15	Hz	74.8	23.3	0.9	1.0	
	GP17	Hz	71.9	23.7	4.0	0.4	
	GP20	Lh	77.3	16.3	6.1	0.3	
	GP21	Hz	85.0	14.4	0.0	0.6	
	GP22	Hz	77.7	17.0	3.8	1.5	
	GP25	Hz	82.2	16.0	1.0	0.8	
	GP28	Lz	73.1	22.5	4.0	0.4	
	GP29	Hz	72.8	22.7	3.8	0.7	
	GP31	Hz	80.1	17.5	1.6	0.8	
	GP34	Lh	71.6	21.3	6.5	0.6	
	GP36	Lh	70.5	22.3	6.2	1.0	
	GP49	Hz	73.1	21.8	4.4	0.7	

Modal compositions are determined by point counting in thin section (1500 points)
Lh lherzolite, *Weh* wehrlite, *Hz* harzburgite

Samples BR218 and BR219 are composite: in BR218 an amphibole-bearing vein (2 mm wide) cuts the lherzolite and in BR219 a cumulate wehrlite adheres to a coarse harzburgite. Amphibole in the vein is idiomorphic, while in the wehrlite poikilitic clinopyroxenes include rounded olivines. Amphibole vein and cumulate wehrlite have blebs of pale yellow glass with microcrystals of clinopyroxene + olivine ± plagioclase. Further details of individual samples are given in Perinelli et al. (1998).

Chemical composition

Whole rocks

Measured compositions fall in the field of worldwide spinel peridotites (Table 2) and define different degrees of melt extraction (Frey and Green 1974; Nickel and Green 1984; Frey et al. 1985). Covariation diagrams show that Al_2O_3 and CaO contents are inversely correlated with MgO (Fig. 2). Relatively higher CaO contents (1.3 wt%; sample GP21) are probably due to the occurrence of secondary calcite. SiO_2, TiO_2 and Na_2O define poor correlations with MgO. The Mg# is rather uniform (90–91.4) and only peridotite domains of composite xenoliths have lower Mg# (86.8), possibly indicating FeO enrichment (Table 2).

Trace element patterns normalised to primitive mantle (McDonough and Sun 1995) show moderate to high incompatible element enrichments (Fig 3a). Xenoliths with incipient pyrometamorphic features show Ba, Nb and Sr negative anomalies while the other samples display high values of Nb, Ta, Zr and a negative Ti anomaly. All samples have concave-upward REE_N with $(Ce/Yb)_N$ ratios between 1.8 and 17.3 (Fig. 3b). The few samples with Nb/Ta negative anomaly inherit these features from clinopyroxene composition.

Olivine

Olivines have a small compositional range (Fo_{89}–Fo_{92}, Table 3). In composite xenoliths, Fo-contents decrease towards the veins (from Fo_{91} to Fo_{86}) due to Mg–Fe exchange reactions between the vein and whole rock. In porphyroclastic samples, olivine neoblasts have lower NiO contents than porphyroclasts (0.10–0.18 and 0.40–0.75 wt%, respectively). Higher CaO contents and low NiO characterize olivine of pyrometamorphic glass patches (Table 3).

Orthopyroxene

This phase generally shows constant compositions ($En_{88.2–91.2}$, $Wo_{1.9–1.8}$, $Fs_{9.9–7}$, Fig. 4) with Mg# values between 89.5 and 93.2, comparable with those of coexisting olivine (Table 3). Al_2O_3 contents decrease from lherzolite to harzburgite, whereas Cr_2O_3 increases (Table 3). In composite xenoliths, orthopyroxene, next to amphibole or wehrlite vein (BR218 and BR219), is enriched in FeO (Mg# = 87.8 and 85.6, respectively) and TiO_2. Chondrite normalised REE patterns of depleted

Table 2 Whole rock compositions of xenoliths from NVL

XRF	BR 213	BR 218	BR 219	GP 5	GP 6	GP 10	GP 14	GP 21	GP 22
SiO_2	44.14	43.99	40.25	42.19	42.60	42.09	44.59	41.84	43.46
TiO_2	0.08	0.04	0.20	0.06	0.05	0.04	0.10	0.21	0.14
Al_2O_3	1.85	2.10	1.73	1.02	0.90	0.92	2.95	1.38	1.15
FeO*	7.70	9.76	11.66	8.59	7.75	7.86	7.15	7.88	7.70
MnO	0.12	0.16	0.18	0.14	0.14	0.13	0.13	0.14	0.14
MgO	43.50	41.26	42.95	44.42	45.10	46.48	41.22	44.62	43.96
CaO	0.98	1.87	1.33	0.82	0.83	0.78	2.51	1.30	0.89
Na_2O	0.17	0.11	0.18	0.19	0.10	0.21	0.33	0.38	0.26
K_2O	0.04	0.03	0.07	0.09	0.07	0.07	0.10	0.14	0.13
P_2O_5	0.02	0.02	0.03	0.05	0.04	0.05	0.03	0.08	0.10
H_2O	0.40		0.07	0.12	0.16	0.27		0.11	0.28
CO_2	0.47		0.10	0.15	0.10	0.19		0.09	0.10
Total	99.47	99.34	98.75	97.84	97.84	99.09	99.10	98.17	98.31
Mg#	90.97	88.28	86.78	90.21	91.21	91.33	91.13	90.99	91.05
ICP-MS									
V	45	76	56	34	30	26	62	37	31
Cr	2975	2395	3096	2611	2715	2666	2883	3184	2601
Co	109.2	104	115	118.8	112.2	118.9	111	108	115.9
Ni	1926	1813	2011	1983	2006	2130	1849	1998	2051
Rb	2.26	1.95	2.68	3.11	3.32	3.26	1.3	3.18	3.4
Sr	18.92	15.1	29.29	38.59	37.47	33.69	11.1	80.51	66.85
Y	1.2	2.66	2.1	1.5	0.8	1.01	1.34	1.6	1.5
Zr	6.08	6	8.14	5.58	5.14	6.05	5.7	6.92	4.23
Nb	1.77	1.23	2.65	1.4	2.33	2.4	0.17	3.4	2.52
Mo	0.87		1.18	1.23	1.41	1.26		1.15	1.34
Cs	0.04	0.33	0.12	0.08	0.06	0.06	0.36	0.13	0.09
Ba	13.18	7.1	20.14	23.93	15.99	21.14	0.68	48.11	39.36
La	1.33	0.79	2.22	3.24	1.68	2.96	0.79	3.05	3.44
Ce	2.64	1.93	4.73	6.49	3.19	3.69	1.84	4.52	3.85
Pr	0.253	0.21	0.458	0.554	0.28	0.382	0.25	0.325	0.331
Nd	1.09	0.88	2.16	2.21	1.1	1.89	0.97	1.91	1.65
Sm	0.27	0.24	0.47	0.46	0.23	0.38	0.17	0.37	0.38
Eu	0.08	0.09	0.179	0.138	0.069	0.115	0.06	0.183	0.145
Gd	0.21	0.35	0.46	0.32	0.15	0.31	0.18	0.33	0.37
Tb	0.03	0.06	0.06	0.05	0.02	0.04	0.03	0.06	0.08
Dy	0.21	0.45	0.36	0.25	0.13	0.23	0.21	0.31	0.38
Ho	0.04	0.1	0.07	0.05	0.03	0.04	0.04	0.08	0.07
Er	0.12	0.28	0.2	0.15	0.08	0.14	0.15	0.17	0.21
Tm	0.023	0.04	0.024	0.018	0.011	0.022	0.02	0.038	0.029
Yb	0.15	0.18	0.16	0.11	0.08	0.09	0.12	0.12	0.12
Lu	0.025	0.04	0.024	0.021	0.012	0.019	0.03	0.018	0.029
Hf	0.24	0.16	0.22	0.16	0.14	0.17	0.11	0.18	0.12
Ta	0.12	0.26	0.195	0.279	0.147	0.238	0.05	0.211	0.25
Tl	0.05	0.01	0.05	0.09	0.04	0.03	0.01	0.03	0.03
Th	0.179	0.13	0.408	0.411	0.183	0.53	0.05	0.934	0.705
U	0.055	0.02	0.092	0.134	0.079	0.199	0.02	0.214	0.182

*FeO** total iron as FeO

samples are enriched in LREE (Fig. 4a, b) and show trace element zoning from core to rim (Fig. 4c). Patterns of more fertile xenoliths (e.g. GP36 or GP42) display a smooth decrease from HREE to LREE (Fig. 4a, b).

Clinopyroxene

CpxI which are mainly diopsidic ($Wo_{44.4-48.2}$, $En_{45.6-52}$, $Fs_{3.6-6.2}$; Table 3) have Mg# values (89.5–94.4) that correlate with the Fo contents of olivine and that are higher than Mg# of coexisting olivine and orthopyroxene. The Al_2O_3, TiO_2 and Na_2O contents decrease with increasing Mg# (Table 3). Pyrometamorphic crystals exhibit a decrease of Al_2O_3 and Na_2O from core to rim. In composite xenoliths clinopyroxene next to veins is enriched in TiO_2 and FeO.

CpxII microlites have higher Cr_2O_3 contents and a more homogeneous Mg# (90.7–93.6) than CpxI (Table 3).

CpxI of different xenoliths reveals marked differences in trace element composition and shows variable enrichments of incompatible elements (Fig. 5a, c, e). Samples GP6, GP32 and GP35 also show intra-mineral zoning (Fig. 5g).

The REE contents (Table 4) allow for the CpxI to be characterized as:

1. Light REE (LREE)-depleted (“not-metasomatized”) clinopyroxenes with $(Ce/Yb)_N$ varying between 0.002

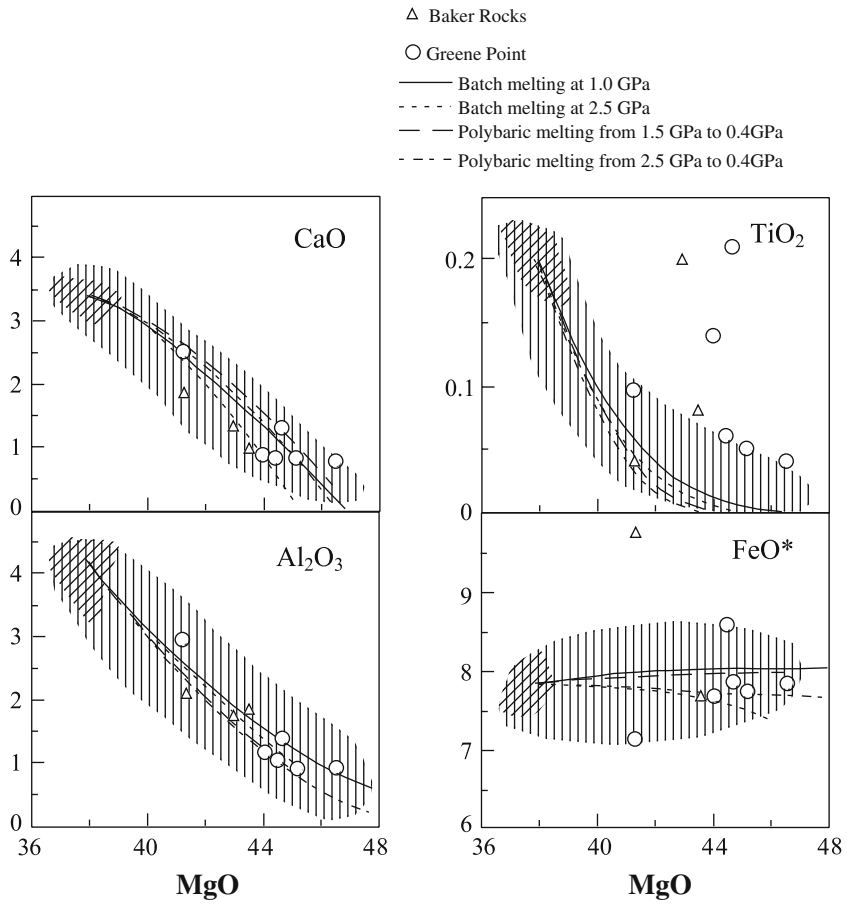

Fig. 2 Concentration of major in NVL xenoliths, plotted with respect to MgO. *Shaded fields* are defined by data of dry spinel peridotite xenoliths from different areas (GERM data repository, http://www.earthref.org/GERM). The *curves* represent the near fractional melting and batch melting trend of a starting source of primitive spinel peridotite using the Niu (1997) model (after Takazawa et al. 2000). Data for primitive mantle (PM) are from McDonough and Sun (1995)

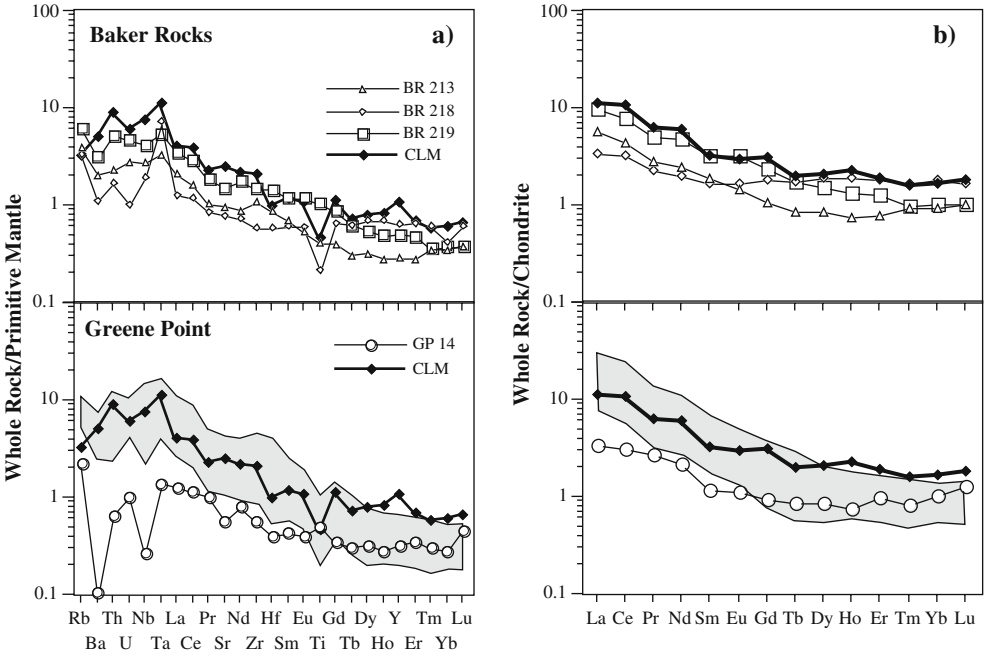

Fig. 3 Incompatible trace element (**a**) and REE (**b**) patterns for spinel peridotites. *Shaded fields* represent the patterns of the remaining GP xenoliths. Trace element plots are ordered according to their decreasing incompatibility during partial melting. Normalizing values after McDonough and Sun (1995). Continental lithospheric mantle (CLM) data are from McDonough (1990)

and 0.58 (n = chondrite normalized value) and Yb_N from 2.9 to 10.8 (Fig. 5d). These clinopyroxenes are depleted in Th,U Nb and Ta with respect to LREE on the primitive normalized diagrams. They also show small to significant Zr and Ti negative anomalies.

Table 3 Representative electron microprobe analyses of olivine, orthopyroxene, clinopyroxene and spinel of a selection of peridotites from northern Victoria Land

	BR 213					BR 218 far from Amph-vein				BR 218* near Amph-vein				BR 218 Amph-vein	
	Ol	Opx	CpxI	CpxII	Sp	Ol	Opx	CpxI	Sp	Ol	Opx	CpxI	Sp	Amph	CpxII
SiO_2	40.47	56.58	52.51	48.67	0.27	40.24	55.38	52.39	0.12	40.25	54.27	51.22		42.72	47.68
TiO_2	0.09	0.16	0.38	1.54	0.02	0.00		0.49	0.23	0.00	0.26	0.82	0.21	3.66	3.01
Al_2O_3	0.00	3.30	5.21	6.19	40.28	0.00	4.00	5.19	49.71	0.21	5.24	5.98	52.65	14.82	7.85
FeO	9.01	5.85	2.55	2.38	12.36	11.97	6.70	2.84	13.62	12.49	7.87	3.42	13.06	4.62	2.93
MnO	0.12	0.09	0.00	0.03	0	0.02		0.18	0.07	0.28		0.09	0.13		0.16
MgO	48.84	32.54	16.24	15.33	18.06	47.31	33.10	15.54	17.98	46.84	31.86	15.31	18.22	16.38	14.43
CaO	0.05	0.92	20.24	22.76		0.07	0.76	21.46		0.05	0.63	21.67		11.68	21.61
Na_2O		0.41	1.66	0.29				1.31				1.08		2.98	0.81
K_2O														0.81	
Cr_2O_3		0.54	1.30	2.23	27.93			0.88	18.16		0.59	0.81	15.98	0.82	1.86
NiO	0.38				0.33	0.35				0.32					
Total	98.96	100.39	100.09	99.42	99.25	99.96	99.94	100.28	99.89	100.44	100.72	100.40	100.25	98.49	100.34
Mg#	90.62	90.84	91.91	91.99	72.26	87.57	89.80	90.70	70.18	86.99	87.83	88.87	71.32	86.34	89.78

	BR 219 far from Wehrlite				BR 219 near from Wehrlite				GP5					GP10	
	Ol	Opx	CpxI	Sp	Ol	Opx	CpxI	Sp	Ol II	Ol	Opx	CpxI	Sp	Ol	Opx
SiO_2	40.04	55.68	51.74	0.07	39.68	55.47	50.74	0.07	39.16	40.72	56.73	53.12	0.1	40.54	56.53
TiO_2	0.01	0.12	0.37	0.16	0.03	0.22	0.90	0.33	0.07	0.05	0.08	0.30	0.03	0.00	0.15
Al_2O_3	0.24	3.75	5.58	46.99	0.04	2.82	6.58	45.49	0.31	0.07	2.91	3.60	39.67	0.13	3.38
FeO	11.65	7.80	3.15	13.93	13.14	9.24	3.39	15.96	15.20	9.39	5.75	2.35	13.24	8.60	5.44
MnO	0.01	0.21	0.15	0.43	0.14	0.13	0.18	0.32	0.15	0.08	0.28	0.09	0.36	0.05	0.19
MgO	46.92	31.41	16.80	17.98	45.61	30.80	15.91	17.02	43.82	49.15	33.35	16.88	17.44	49.75	32.84
CaO	0.09	0.94	20.19		0.09	0.95	20.41		0.26	0.08	0.71	22.26		0.07	0.89
Na_2O		0.47	1.12			0.48	1.45		0.10		0.44	0.82			0.51
Cr_2O_3		0.58	1.12	19.44		0.54	1.12	20.74			0.58	0.99	29.15		0.71
NiO	0.49			0.41	0.45			0.32		0.49			0.54	0.48	
Total	99.45	100.96	100.22	99.41	99.18	100.65	100.68	100.25	99.07	100.03	100.83	100.41	100.53	99.62	100.64
Mg#	87.78	87.77	90.48	69.71	86.09	85.60	89.32	65.53	83.71	90.32	91.18	92.76	70.14	91.16	91.50

	GP10				GP14					GP16					GP28
	CpxI core	CpxI rim	CpxII	Sp	Ol	Opx	CpxI	CpxII	Sp	Ol n	Ol p	Opx	CpxI	Sp	Ol
SiO_2	52.77	53.18	53.02	0.19	40.93	54.95	52.09	52.91	0.1	41.37	40.29	55.58	52.44	0.29	41.13
TiO_2	0.52	0.65	0.79	0.49	0.04	0.15	0.48		0.09	0	0.06	0.06	0.24	0.24	
Al_2O_3	5.06	2.93	2.78	38.09	0.25	5.43	6.69	3.42	56.45	0	0	3.3	3.99	34.09	
FeO	2.55	2.50	2.17	11.99	9.75	6.11	2.74	2.36	9.83	8.97	9.37	5.65	2.68	11.41	9.03
MnO			0.06	0.58	0.33	0.17	0.16	0.00		0.35	0.29	0.14	0.16	0.2	
MgO	16.48	17.67	17.05	17.37	49.13	31.37	15.52	16.23	20.63	49.92	48.17	32.37	16.78	17.34	50.2
CaO	20.68	21.82	22.10		0.08	0.91	19.84	22.73		0.13	0.07	1.07	21.04		
Na_2O	1.47	0.69	0.85			0.53	1.60	0.79				0.5	0.92		
Cr_2O_3	1.32	1.61	1.60	30.92		0.57	0.95	0.88	12.09			0.85	1.52	35.75	
NiO				0.3	0.41					0.18	0.75			0.33	0.38
Total	100.85	101.05	100.42	99.93	100.92	100.19	100.07	99.32	99.21	100.92	99.00	99.52	99.77	99.65	100.74
Mg#	92.01	92.65	93.34	72.09	89.98	90.15	90.99	92.45	79.85	90.84	90.16	91.08	91.78	73.04	90.84

	GP28			GP29				GP34				GP49			
	Opx	CpxI	Sp	Ol	Opx	CpxI	Sp	Ol	Opx	CpxI	Sp	Ol	Opx	CpxI	Sp
SiO_2	55.78	52.36		41.17	55.51	52		40.74	55.00	51.79		41.12	55.17	52.29	
TiO_2						0.21				0.18				0.2	
Al_2O_3	3.37	4.33	36.73		2.96	4.19	41.6		4.23	5.66	49.03		3.35	3.57	37.33
FeO	5.36	2.12	13.4	9.37	6.29	2.39	13.15	8.82	5.41	2.41	10.51	9.51	5.89	2.34	13.14
MnO								0.11							
MgO	34.34	16.17	17.54	49.96	34.55	16.72	17.88	49.33	33.81	16.46	19.6	49.73	34.18	16.88	17.04
CaO	0.94	21.02			0.69	22.16			0.92	20.67			0.87	22.65	
Na_2O		1.4				0.89				1.3				0.71	
Cr_2O_3	0.66	1.59	32.41		0.55	1.23	27.66		0.54	1.3	20.66		0.64	1.07	32.23
NiO				0.32				0.5				0.38			
Total	100.45	98.99	100.08	100.82	100.55	99.79	100.29	99.50	99.91	99.77	99.80	100.74	100.10	99.71	99.74
Mg#	91.95	93.15	70.00	90.48	90.73	92.58	70.80	90.89	91.76	92.41	76.88	90.31	91.19	92.79	69.81

CpxI primary clinopyroxene, *CpxII* pyroxene crystallised in the glass, *p* porphiroclast, *n* neoblast crystal

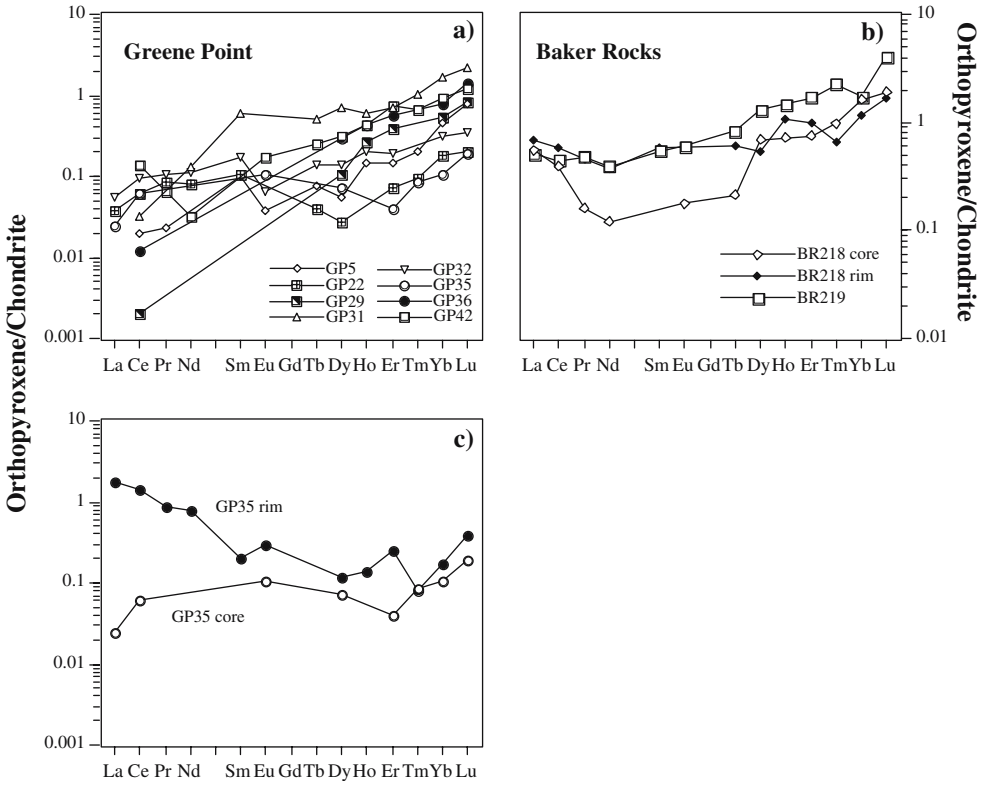

Fig. 4 Incompatible trace element plot for orthopyroxene of NVL xenoliths. Primitive mantle normalizing values are after McDonough and Sun (1995)

2. LREE-enriched clinopyroxenes ("metasomatized") with $1 < (Ce/Yb)_N < 19$ (Fig. 5b, f). They show a wider range of heavy REE (HREE) contents ($Yb_N = 1.2–11.8$). The chondrite normalized REE patterns vary from convex-upward (GP10, BR213 and BR218*) to "spoon shaped", that is enriched in LREE relative to middle REE (GP6, BR218; Fig. 5b, f). The primitive normalized diagrams for these clinopyroxenes show small or not positive anomalies of U and slight to marked negative anomalies of Nb (but not for Ta), Zr and/or Hf, and Ti. In this group, sample GP5 differs from the other clinopyroxenes for the relatively flat distribution of Th to Lu, with positive U anomaly (Fig. 5). CpxII, large enough to be analysed, has been found in one sample (BR213) and shows a trace element pattern similar to that of CpxI (Fig. 5).

Spinel

Spinel displays wide compositional variability (Table 3) with Cr# $[(Cr/Cr + Al + Fe^{3+})\times100]$ gradually increasing from 12 to 60 from lherzolites to harzburgites. The negative correlation between Mg# and Cr# (Fig. 6) suggests that partial melting strongly controls the spinel composition. In composite xenoliths, spinel shows relatively low Mg# and Cr# which is indicative of iron enrichment, a trend commonly associated with metasomatic effects (Dawson 1984).

Amphibole

Major and trace element contents of euhedral pargasite from the amphibole vein in BR218 are given in Tables 3 and 4. With respect to amphibole occurring in peridotite xenoliths from McMurdo Volcanic Group (Hornig et al. 1991; Beccaluva et al. 1991; Gamble et al. 1988; Coltorti et al. 2004), BR218 pargasite has lower Ti and alkali contents and higher Al_2O_3 values.

Chondrite normalized trace element patterns display positive Nb and Sr anomalies and a slight negative Zr anomaly. The convex-upward LREE-enriched patterns resemble those of megacrysts formed as a liquidus phase from alkaline magmas (Irving and Frey 1984; Fig. 7).

Glass

Glass patches are practically ubiquitous: at Green Point they are Si-rich and alkaline with Phonolite–Nepheline Trachyte compositions (Table 5). Glass blebs in BR213 are subalkaline and Quartz-normative and have Latite composition. Glasses show unusually high Mg# independently from their silica contents (0.82 in alkaline glasses and 0.79 in sub-alkaline ones). In composite xenoliths, glass compositions range from Mugearite to Benmoreite and show lower Mg# (from 0.69 to 0.53).

Both alkaline and subalkaline glasses are enriched in LREE but differ for MREE and HREE contents; the REE_N patterns are fractionated in subalkaline glasses

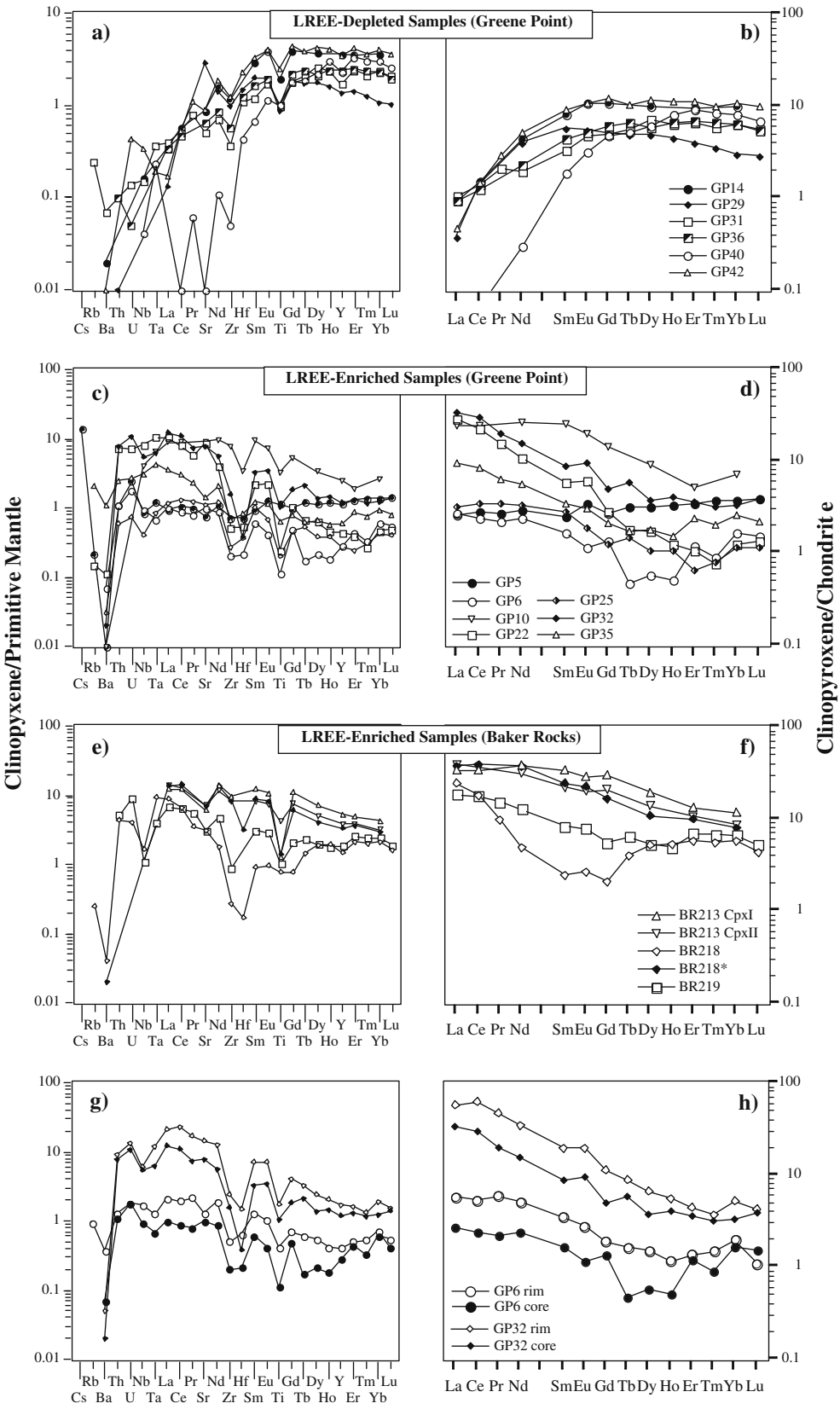

Fig. 5 Trace element and REE patterns of clinopyroxene, normalized to primitive mantle and chondrite, respectively (McDonough and Sun 1995). *Clinopyroxene near amphibole vein.

and almost flat in alkaline ones (Fig. 8; Table. 6). Alkaline and subalkaline PM-normalized diagrams are both characterized by positive Rb and Zr anomalies. Glass in amphibole vein of BR218 sample is enriched in Nb and exhibits a trace element pattern similar to the nephelinite SAX20, the Greene Point host lava, and to

Table 4 LAM ICP-MS analyses (ppm) of clynopyroxene, orthopyroxene and amphibole separates

	Cpx																					
	GP5[a] Core	GP5[a] rim	GP6[a] core	GP6[a] rim	GP10[a,b] core	GP14[b] core	GP22[a] core	GP22[a] rim	GP25[a] Core	GP25[a] rim	GP28 core	GP28 rim	GP29	GP29	GP31 Core	GP31 rim	GP32[a] core	GP32[a] rim	GP34 core	GP34 rim	GP35[a] core	GP35[a] rim
V	234	245	178	183			189	200	159	155					213	211	202	255			181	190
Rb	0.12	0.09		0.54			0.09			0.11					0.15						1.28	1.55
Sr	14.94	17.11	19.61	25.63	179	17.16	171	164	21.79	23.18	42.28	41.59	56.54	57.67	10.15	12.00	155	289	12.49	15.91	28.02	65.08
Y	4.82	5.49	1.20	1.73	10.56	15.36	1.91	2.04	1.17	1.35	9.24	9.57	5.79	6.25	7.29	8.74	5.11	7.31	11.22	12.16	2.52	4.61
Zr	7.49	8.58	2.13	5.27	81.85	12.04	5.48	5.92	2.79	2.90	20.07	19.93	10.24	11.23	3.90	3.75	16.36	25.05	6.51	8.23	7.11	18.64
Nb	0.55	0.77	0.62	1.11	2.68	0.11	5.31	5.45	0.26	0.25					0.10	0.13	3.59	4.01			2.03	4.12
Cs	0.29																					
Ba	0.05		0.47	2.43	0.08	0.14	0.76	0.08	0.21	0.26					0.45		0.16	0.31			7.03	22.32
La	0.61	0.73	0.63	1.37	5.75	0.22	6.76	6.87	0.75	0.88	0.32	0.32	0.09	0.05	0.25	0.26	7.96	13.52	0.32	0.24	2.29	4.4
Ce	1.74	2.03	1.46	3.23	14.84	0.95	13.47	13.36	2.14	2.27	1.52	1.46	0.82	0.82	0.86	0.97	18.40	38.04	0.97	0.77	5.09	10.67
Pr	0.25	0.33	0.20	0.55			1.44	1.43	0.31	0.34					0.20	0.19	1.85	4.36			0.58	1.43
Nd	1.35	1.64	1.07	2.34	12.15	1.99	4.93	5.21	1.48	1.77	2.42	2.50	1.78	1.64	0.89	1.59	7.07	15.86	1.20	1.08	2.54	6.31
Sm	0.37	0.60	0.25	0.52	3.79	1.20	0.87	0.91	0.41	0.41	0.91	0.90	0.81	0.68	0.49	0.85	1.32	2.91	0.70	0.63	0.50	1.2
Eu	0.19	0.20	0.06	0.16	1.11	0.60	0.35	0.37	0.11	0.12	0.40	0.40	0.30	0.34	0.27	0.25	0.53	1.11	0.33	0.32	0.17	0.42
Gd	0.53	0.75	0.26	0.37	2.87	2.10	0.56	0.59	0.25	0.25	1.35	1.10	0.97	1.02	0.99	1.04	0.99	2.22			0.42	1.26
Tb	0.12	0.14	0.02	0.06			0.07	0.09	0.05	0.03			0.17	0.19	0.20	0.25	0.21	0.32		0.23	0.06	0.16
Dy	0.77	0.92	0.14	0.37	2.26	2.48	0.42	0.39	0.26	0.32	1.33	1.60	1.19	1.08	1.75	1.97	0.93	1.64	2.01		0.45	0.99
Ho	0.18	0.21	0.03	0.06			0.07	0.09	0.06	0.06	0.36	0.38	0.24	0.22	0.35	0.34	0.22	0.30	0.41	0.43	0.08	0.22
Er	0.56	0.69	0.19	0.22	0.82	1.53	0.17	0.20	0.11	0.16	0.80	1.01	0.62	0.63	1.04	0.92	0.58	0.71	1.00	1.38	0.38	0.61
Tm	0.09	0.12	0.02	0.04			0.02	0.02	0.02	0.03	0.14	0.14	0.08	0.08	0.15	0.15	0.08	0.09	0.17	0.20	0.05	0.1
Yb	0.60	0.62	0.27	0.32	1.14	1.59	0.21	0.19	0.19	0.20	0.80	0.90	0.47	0.58	1.03	1.02	0.54	0.83	1.20	1.02	0.41	0.69
Lu	0.09	0.11	0.04	0.03			0.03	0.04	0.03	0.02	0.09	0.12	0.07	0.08	0.14	0.1	0.1	0.10	0.19	0.14	0.05	0.09
Hf	0.20	0.25	0.06	0.18	0.94		0.15	0.17	0.10	0.08	0.50	0.36	0.42	0.29	0.31	0.3	0.11	0.42	0.34	0.51	0.23	0.52
Ta	0.04	0.04	0.03	0.05	0.24		0.39	0.43	0.03	0.03					0.01	0.01	0.23	0.44			0.16	0.25
Th	0.09	0.10	0.08	0.10			0.58	0.52	0.05	0.03	0.02	0.01				0.01	0.61	0.72	0.01		0.20	0.34
U	0.05	0.06	0.04	0.04			0.15	0.12	0.01	0.02							0.22	0.27			0.05	0.1

	Cpx														Opx							
	GP36 Core	GP36 rim	GP40 core	GP40 rim	GP47 core	GP47 rim	GP49 core	GP49 rim	BR213[a,b] core	BR218[a] core	BR218[a] rim	BR218[a,b,c]	BR219[a] core	BR219[a] rim	GP5 core	GP5 rim	GP6 core	GP6 rim	GP10[b] core	GP14[b] core	GP22 Core	GP22 rim
V			209	245	241	231				258	228		258	253	72.81	68.36	61.74	60.79			51.56	51.53
Rb										0.15					0.63	0.029	0.071	0.102				
Sr	12.77	11.56	0.22		17.47	15.72	33.82	33.09	122	61.56	53.25	138	61.93	69.71	8.96		0.097	1.45	0.34	0.138	0.28	0.36
Y	10.29	10.03	9.8	9.70	14.81	13.88	7.99	6.94	22.75	6.41	5.74	14.43	7.98	9.42	0.47	0.29	0.049	0.11	1.1	0.95	0.089	0.117
Zr	6.06	5.65	0.51	0.99	12.79	12.50	13.61	12.20	102	2.85	1.90	84.70	9.37	19.84	2.64	0.2	0.131	0.56	2.1	1.57	0.145	0.29
Nb			0.02	0.09	0.22	0.21	0.24			1.09	1.03	0.73	0.72	0.56	0.66	0.010	0.041	0.17	0.078	0.015	0.22	0.23
Cs															0.025	0.012						
Ba					0.08					0.28		0.11		0.22	5.42	0.26		0.88				
La	0.22	0.18			0.11	0.12	0.32	0.28	7.92	5.79	5.28	8.81	4.39	5.98	1.11		0.004	0.11			0.009	0.019
Ce	0.77	0.71	0.01		0.89	0.89	1.50	1.46	20.58	10.95	9.73	24	10.74	12.04	2.07	0.012	0.038	0.27			0.038	0.043
Pr			0.02	0.02	0.27	0.28				0.90	0.79		1.41	1.74	0.2	0.002	0.007	0.023			0.008	0.009
Nd	1.06	0.86	0.14	0.21	2.35	2.22	2.04	2.3	17.36	2.25	2.11	17.21	5.87	6.99	0.45		0.011	0.1	0.063	0.02	0.037	0.054
Sm	0.65	0.46	0.28	0.29	1.35	1.24	0.73	0.75	5.02	0.36	0.30	3.6	1.24	1.51	0.07	0.015		0.025	0.036	0.012	0.016	0.006
Eu	0.29	0.19	0.18	0.17	0.61	0.57	0.35	0.35	1.63	0.15	0.12	1.26	0.44	0.66	0.031	0.002						0.003

Table 4 (Contd.)

	Cpx														Opx							
	GP36 Core	GP36 rim	GP40 core	GP40 rim	GP47 core	GP47 rim	GP49 core	GP49 rim	BR213[a,b] core	BR218[a] core	BR218[a] rim	BR218[a,b,c]	BR219[a] core	BR219[a] rim	GP5 core	GP5 rim	GP6 core	GP6 rim	GP10[b] core	GP14[b] core	GP22 Core	GP22 rim
Gd	1.20	1.09	0.96	0.81	2.38	1.88	1.20	1.08	5.95	0.42	0.57	3.29	1.11	1.36	0.07	0.026	0.04	0.017	0.07	0.051		
Tb	0.24	0.2	0.18	0.26	0.37	0.35	0.23	0.24		0.14	0.14		0.23	0.29	0.011	0.003	0.002	0.005			0.001	0.003
Dy	1.42	1.29	1.49	1.69	2.85	2.94	1.43	1.39	4.79	1.27	0.95	2.69	1.30	1.90	0.065	0.013		0.035	0.11	0.099	0.007	0.013
Ho	0.36	0.32	0.45	0.46	0.61	0.61	0.32	0.25		0.29	0.25		0.27	0.35	0.02	0.008		0.004				0.002
Er	1.08	1.06	1.46	1.00	1.82	1.77	1.02	0.61	2.13	0.92	0.97	1.61	1.11	1.33	0.075	0.024	0.024	0.017	0.096	0.13	0.012	0.014
Tm	0.16	0.14	0.21	0.16	0.25	0.27	0.13	0.11		0.14	0.13		0.17	0.17	0.01	0.005		0.006			0.002	0.005
Yb	1.02	0.93	1.31	1.54	1.74	1.75	0.68	0.66	1.9	0.93	0.88	1.29	1.07	0.96	0.069	0.072	0.03	0.041	0.15	0.21	0.029	0.022
Lu	0.13	0.14	0.17	0.2	0.24	0.26	0.10	0.13		0.11	0.11		0.13	0.15	0.013	0.019	0.002	0.006	0.034	0.04	0.005	0.005
Hf	0.35	0.22	0.12	0.1	0.64	0.68	0.44	0.71	1.22	0.05	0.04	0.9		0.18	0.085	0.005			0.081	0.044	0.012	0.009
Ta			0.01		0.01					0.34	0.27	0.14	0.15	0.11	0.036			0.009			0.002	0.004
Th	0.01					0.01		0.00		0.35	0.34		0.41	0.68	0.15	0.007	0.002	0.03				0.008
U				0.01	0.01	0.01				0.08	0.09		0.19	0.26	0.033	0.001	0.001	0.011			0.003	0.23

	Opx																			Amph	
	GP25 Core	GP25 rim	GP28	GP29	GP31 core	GP31 rim	GP32 core	GP32 rim	GP35 core	GP35 rim	GP36	GP40 core	GP40 rim	GP42 core	GP42 rim	GP49	BR218 core	BR218 rim	BR219 core	BR219 rim	BR218[b] Core	BR218[b] rim
V	51.21	47.82	87.04	99.04	105	121	63.26	56.98	61.32	64.39	88.41	68.72	65.06	76.32	69.42	108	116	126	166	209	416	407
Rb									0.51	0.36		0.029	0.019								3	3
Sr	0.067	0.04		0.11		0.2	0.258	0.35	6.83	5.37			0.024			0.11	2.01	2.53	1.01	0.81	895	895
Y	0.102	0.068	0.54	0.47	0.84	1.01	0.319	0.305	0.26	0.221	0.84	0.38	0.33	0.67	0.58	0.63	0.84	0.8	1.61	1.77	32	32
Zr	0.34	0.198	1.05	0.74	0.29		0.81	0.71	1.87	1.58	0.40			0.6	0.53	1.43	0.2	0.95	2.98	5.66	163	160
Nb	0.032	0.03					0.067	0.082	0.78	0.61		0.005	0.005	0.012	0.006		0.19	0.076	0.08	0.06	96	85
Cs								0.021							0.014							
Ba	0.08					0.36		0.058	4.48	3.95		0.036	0.14								316	315
La		0.004					0.013	0.013	0.48	0.43							0.13	0.16	0.12	0.17	17.6	16.5
Ce	0.009	0.004		0.00	0.02		0.058	0.068	1.09	0.87	0.01		0.003	0.087	0.003	0.02	0.24	0.35	0.27	0.23	46.9	45.8
Pr		0.005					0.010	0.009	0.101	0.081				0.0059	0.003		0.015	0.042	0.045	0.018		
Nd	0.012	0.006			0.061		0.052	0.08	0.34	0.35				0.015	0.026	0.02	0.055	0.17	0.18	0.19	36.2	36.3
Sm	0.008				0.087		0.025	0.036	0.051	0.03			0.004		0.007			0.085	0.08		9.6	8.6
Eu		0.005				0.09	0.004		0.021	0.017		0.0094		0.010	0.009		0.01		0.034		2.88	2.72
Gd	0.064						0.061		0.074	0.064				0.069	0.026					0.31	8.2	8.2
Tb		0.002			0.018		0.005	0.008	0.002			0.003	0.003	0.009	0.012		0.008	0.022	0.03	0.016		
Dy	0.015		0.04	0.03	0.17	0.066	0.034	0.034	0.034	0.029	0.07	0.041	0.027	0.077	0.086	0.08	0.17	0.062	0.32	0.31	6.6	6.7
Ho	0.004	0.006		0.01	0.033	0.049	0.011	0.008	0.005	0.008	0.02	0.015	0.012	0.023	0.020	0.03	0.039	0.058	0.08	0.09		
Er	0.010	0.005	0.07	0.06	0.11	0.12	0.03	0.028	0.0302	0.04	0.09	0.055	0.059	0.121	0.096	0.09	0.121	0.16	0.27	0.49	3.3	2.81
Tm	0.001	0.003			0.025	0.042	0.013	0.003	0.004	0.002		0.013	0.009	0.016	0.019	0.02	0.024	0.016	0.056	0.043		
Yb	0.036	0.011	0.18	0.09	0.27	0.28	0.051	0.065	0.061	0.028	0.13	0.115	0.107	0.149	0.136	0.18	0.26	0.19	0.28	0.36	2.88	2.93
Lu	0.005	0.008	0.02	0.02	0.055	0.068	0.008	0.013	0.014	0.009	0.04	0.022	0.014	0.029	0.025	0.05	0.047		0.1	0.07		
Hf	0.010	0.011			0.035		0.005	0.005	0.033	0.045	0.04	0.013	0.011	0.034	0.018	0.05	0.016			0.25		
Ta					0.027		0.006	0.006	0.048	0.038		0.004					0.019	0.039				
Th	0.001						0.003	0.002	0.065	0.059	0.003		0.001	0.001			0.049	0.09	0.1	0.2		
U	0.065	0.001					0.001	0.002	0.021	0.025		0.001					0.012	0.006	0.038	0.04		

[a]Metasomatised sample
[b]Trace elements data determined by SIMS
[c]Clinopyroxene near amphibole vein

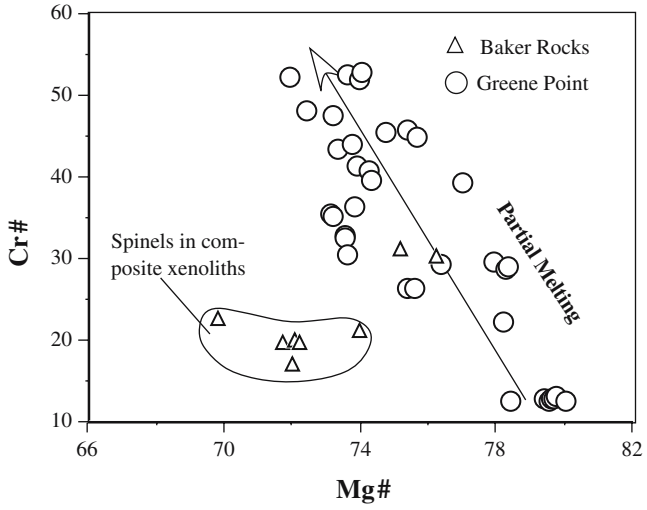

Fig. 6 Composition of spinel in terms of Mg# [(Mg/Mg + Fe^{2+})×100] and Cr# [(Cr/Cr + Al + Fe^{3+})×100]. The plot illustrates a negative correlation between the two parameters. More depleted xenoliths have higher Cr# suggesting a primary composition control by partial melting

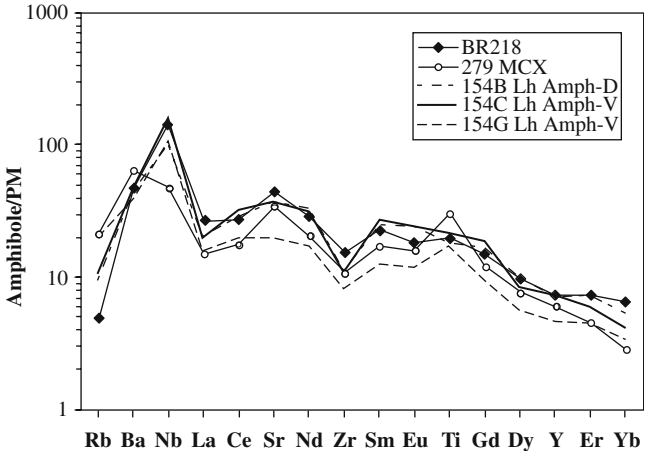

Fig. 7 Primitive mantle (PM; McDonough and Sun 1995) normalized incompatible trace elements distribution of amphibole. The composition of amphibole megacryst (279 MCX), Beccaluva et al. (1991) and disseminated amphibole (amph-D) and amphibole in vein (amph-V) from Coltorti et al. (2004) are also reported

glasses in a composite lherzolite described by Coltorti et al. (2004; Fig. 8).

Oxygen isotope composition

Olivine

Olivine in anhydrous spl-lherzolites exhibits constant O-isotope composition ($\delta^{18}O_{Ol}$ = 5.4 ± 0.19‰; Table 7), in the range of spinel-lherzolites on a worldwide scale (5.19 ± 0.28;. Mattey et al. 1994). Only sample GP49 shows an anomalously high $\delta^{18}O_{Ol}$ (5.81‰). The $\delta^{18}O$ values are consistent with the homogenous Fo contents. Olivine grains from composite xenoliths show a variable O-isotope composition (5.0–5.8‰); those from the amphibole-bearing sample (BR 218) have higher $\delta^{18}O$ values (5.7–5.8‰) regardless of whether they were collected from domains adjacent to amphibole or from anhydrous domains. Olivines from samples BR213 and 219 show the lowest $\delta^{18}O$ values measured in this suite of xenoliths (5.0–5.1‰).

Orthopyroxene

Enstatite in peridotite xenoliths has homogeneous $\delta^{18}O$ values (5.8 ± 0.16‰; Table 7); the $\Delta^{18}O_{opx\text{-}ol}$ values ($\delta^{18}O_{enstatite}$-$\delta^{18}O_{olivine}$) are quite variable ($\Delta^{18}O_{ol\text{-}opx}$ 0.48 ± 0.30‰) with respect to the 0.5‰ equilibrium fractionation at mantle conditions (Mattey et al. 1994). The highest $\delta^{18}O$ values (6.1‰) are found in amphibole-bearing sample.

Clinopyroxene

Clinopyroxenes have heterogeneous $\delta^{18}O$ values ranging from 5.0 to 5.7‰, the highest $\delta^{18}O$ values shown by cpx from amphibole bearing sample. Clinopyroxene–olivine fractionation ($\Delta^{18}O_{ol\text{-}cpx}$ −0.07 ± 0.19‰) indicates O-isotope disequilibrium (Fig. 9a). Among not-metasomatized samples, the $\delta^{18}O_{cpx}$ values inversely correlate with Mg# and Cr_2O_3 contents (R^2 = 0.709 and 0.595, respectively). Positive covariations are observed for the $\delta^{18}O_{cpx}$ versus TiO_2 (R^2 = 0.727) and versus Y (R^2 = 0.527) (Fig. 9e–f), whereas poor or no correlations are found for the metasomatic ones (R^2 = 0.318 and 0.086, respectively). Poor covariation trends ($R^2 \leq 0.277$) are displayed by either group in the $\delta^{18}O_{cpx}$ versus SiO_2, (Fig 9d), and in the $\delta^{18}O_{cpx}$ versus Al_2O_3, versus La, and versus Ce.

Spinel

The measured oxygen isotope compositions of spinel are variable (3.2–4.9‰; Table 7) and within the values reported for mantle spinel worldwide (e.g. Kyser et al. 1981; Chazot et al. 1997). Due to the paucity of samples (n = 4), the $\delta^{18}O_{spl}$ correlations are poorly constrained; however, a remarkable positive covariation occurs between the $\delta^{18}O_{spl}$ values and spinel Cr# (R^2 = 0.953)

Discussion

Variations in modal composition, whole rock and mineral chemistry provide the evidence for heterogeneous upper mantle beneath northern Victoria Land which is due to the combined effects of partial melting and metasomatic enrichments.

Table 5 Electron microprobe analyses of intergranular glasses in peridotites from northern Victoria Land

	BR213				BR218		BR219			MB 33 BR Host Lava	GP1		GP5	GP6	GP10			GP14				GP22		SAX20 GP Host Lava
SiO_2	60.22	61.03	61.82	60.93	53.89	55.25	49.44	50.75	49.37	45.92	57.68	57.65	61.45	63.20	61.7	58.74	58.58	62.88	62.90	63.30	63.12	58.60	58.17	41.23
TiO_2	1.27	1.29	1.19	1.22	5.34	5.12	3.96	3.39	3.84	2.83	0.26	0.23	0.63	0.59	0.57	0.65	0.91	0.84	0.27	0.42	0.38	0.91	0.89	3.69
Al_2O_3	18.24	18.99	19.35	19.34	15.83	16.50	18.63	18.78	18.70	15.39	21.79	22.15	20.10	19.10	21.14	22.52	21.23	18.2	19.99	20.06	20.16	19.81	18.82	12.05
FeO	2.17	2.01	2.14	2.16	3.99	4.04	7.74	6.16	7.45	11.27	0.89	1.27	1.07	1.04	0.89	1.13	0.99	1.33	0.80	0.59	0.73	1.64	1.97	14.80
MnO					0.19	0.11	0.09	0.20	0.00	0.17												0.14	0.12	0.29
MgO	4.59	3.73	2.91	2.95	4.98	4.80	4.80	4.75	4.75	10.27	1.98	1.03	1.71	1.14	0.43	1	1.34	3.38	0.32	0.31	0.41	1.63	3.47	9.52
CaO	5.83	5.86	6.06	6.06	7.66	7.51	10.45	10.58	10.82	8.57	2.35	1.12	1.54	0.54	0.95	0.51	1.55	0.83	0.97	0.86	0.72	1.74	3.88	9.41
Na_2O	3.71	2.94	3.71	3.86	4.10	3.70	2.80	2.53	2.91	3.60	8.75	9.16	7.14	7.23	7.05	9.06	8.01	5.77	6.91	7.21	7.07	8.15	7.91	5.42
K_2O	2.47	2.51	2.44	2.48	1.95	2.10	1.12	1.36	1.10	1.26	6.19	6.5	6.58	6.62	7.3	6.77	6.72	6.82	6.82	6.73	6.81	5.84	5.11	1.57
P_2O_5			0.22		1.06	1.01	0.67	0.79	0.69	0.52			0.62	0.38			0.76					0.44		1.63
Total	98.50	98.36	99.84	99.00	98.96	100.12	99.69	99.29	99.63	99.80	99.89	99.11	100.84	99.84	100.03	100.38	100.09	100.05	98.97	99.48	99.40	98.90	100.34	99.61
Mg#	0.79	0.77	0.71	0.71	0.69	0.68	0.53	0.58	0.53	0.62	0.80	0.59	0.74	0.66	0.46	0.61	0.71	0.82	0.41	0.48	0.50	0.64	0.76	0.53
Q	10.47	16.36	13.96	11.90	4.42	7.10	1.84	4.21	1.12	0.00	0.00	0.00	0.00	0.00	0.00	0.00	0.00	0.00	0.00	0.00	0.00	0.00	0.00	0.00
C	0.00	0.79	0.11	0.00	0.00	0.00	0.00	0.00	0.00	0.00	0.00	0.00	0.00	0.00	0.00	0.00	0.00	0.00	0.00	0.00	0.00	0.00	0.00	0.00
or	14.81	15.07	14.43	14.79	11.60	12.39	6.64	8.09	6.52	7.45	36.61	38.74	38.54	39.17	43.11	39.84	39.66	40.26	40.71	39.97	40.47	34.87	30.07	9.28
ab	31.85	25.28	31.43	32.97	34.98	31.22	23.72	21.54	24.68	19.12	25.04	26.93	42.44	50.06	38.74	29.57	33.54	46.54	46.68	47.55	47.25	38.06	30.90	5.61
an	26.20	29.54	28.66	28.39	19.23	22.15	35.01	36.09	34.80	22.11	1.90	0.13	3.33	0.11	4.47	0.78	2.12	3.62	3.42	2.51	3.18	0.22	0.75	3.92
ne	0.00	0.00	0.00	0.00	0.00	0.00	0.00	0.00	0.00	6.15	26.57	27.76	9.45	6.07	11.31	25.34	18.50	1.21	6.71	7.46	7.00	17.13	19.37	21.82
di	2.46	0.00	0.00	1.54	4.65	2.29	10.05	9.22	11.63	13.74	7.67	4.39	0.18	0.07	0.18	1.35	0.06	0.39	1.14	1.39	0.32	4.40	14.46	26.09
hy	10.92	9.68	7.81	7.23	10.35	10.86	11.75	11.02	10.50	0.00	0.00	0.00	0.00	0.00	0.00	0.00	0.00	0.00	0.00	0.00	0.00	0.00	0.00	0.00
ol	0.00	0.00	0.00	0.00	0.00	0.00	0.00	0.00	0.00	22.09	1.26	0.98	2.91	2.01	0.69	1.32	2.32	5.77	0.42	0.09	0.68	1.71	1.78	17.43
mt	0.85	0.79	0.83	0.84	0.00	0.00	1.91	1.52	1.84	2.77	0.45	0.64	0.53	0.52	0.33	0.56	0.00	0.52	0.40	0.09	0.37	0.83	0.98	5.07
Il	2.45	2.49	2.26	2.34	6.87	6.70	7.53	6.48	7.31	5.37	0.49	0.44	1.19	1.12	1.08	1.23	1.44	1.59	0.52	0.80	0.73	1.75	1.68	7.01
ap	0.00	0.00	0.51	0.00	2.47	2.33	1.56	1.84	1.60	1.20	0.00	0.00	1.42	0.88	0.00	0.00	1.76	0.00	0.00	0.00	0.00	1.03	0.00	3.78

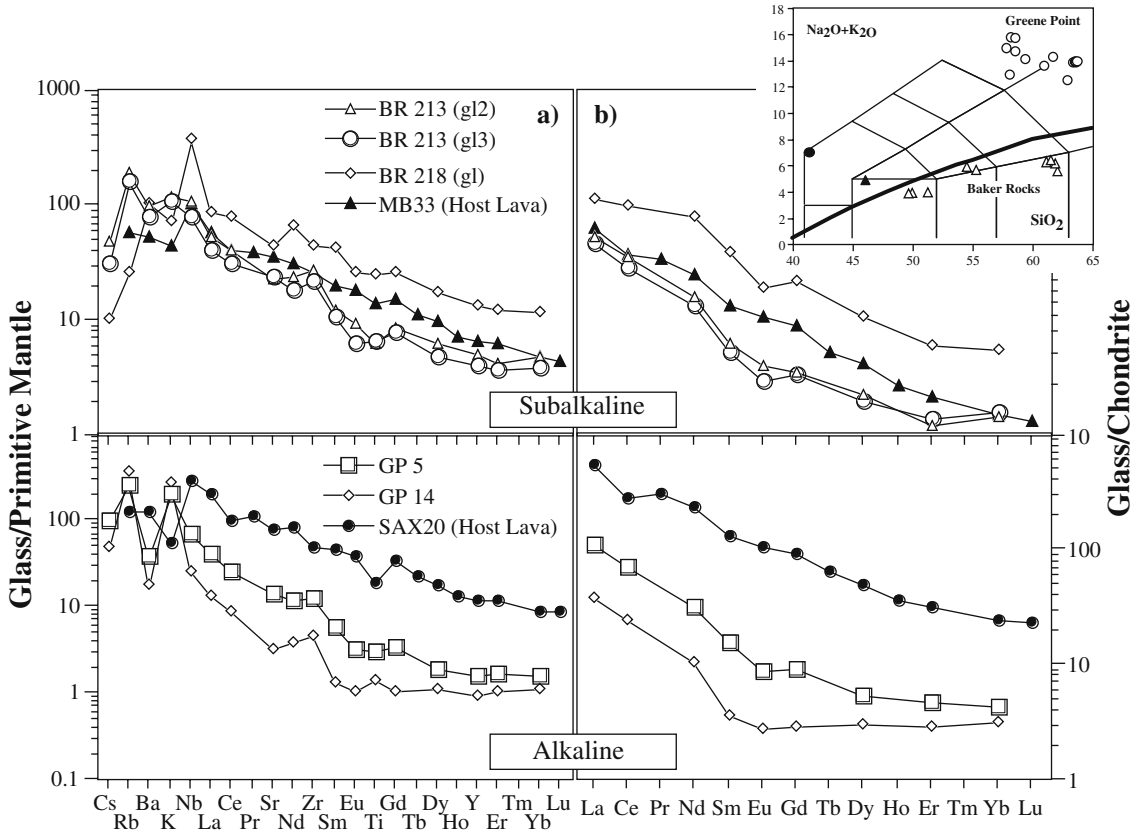

Fig. 8 Classification of glass included in Baker Rocks and Greene Point xenoliths after Le Bas et al. (1986). Discriminating curve of alkaline and subalkaline field is from Irvine and Baragar (1971). Chondrite normalized trace element patterns (**a**) and REE pattern (**b**) for glasses

Extraction of silicate melts, resulting from different degrees of partial melting, may account for: (1) decrease of clinopyroxene modal proportion; (2) whole rock and pyroxene depletion in "basaltic" components (e.g. Al, Na, REE), and (3) contemporaneous build up of refractory elements (e.g. MgO, Ni, Cr# of pyroxene and spinel; Table 2, 3). In the following discussion, we distinguished metasomatized versus not-metasomatized samples according to the occurrence of LREE-enrichment or LREE-depletion in clinopyroxene (Table 4).

Partial melting

Whole rock major element compositions define trends similar to those calculated for residuals of the primitive mantle melting (Niu 1997) in the spinel stability field (Fig. 2). Spinel Cr# of the xenoliths varies between 0.13 and 0.53 (Table 3) and constrains the extent of source melting to be 3–17% of perfect fractional melting in the spinel stability field (Hellebrand et al. 2001). For most samples, clinopyroxene HREE contents confirm that fractional melting occurred in the spinel stability field (e.g. Johnson et al. 1990; Norman 1998; Xu et al. 2000; Hellebrand et al. 2002). The degree of melting (*F*) varies between 3 and 18% (Fig. 10a). However, the fractionated HREE patterns of samples GP40, BR218 and GP6 likely indicate a garnet-bearing mantle residue. In order to produce the observed HREE abundances, an initial 5–20% of melting into the garnet stability field needs to be accounted for, then followed by

Table 6 SIMS analyses (ppm) of intergranular glasses

	GP 5	GP 14	BR 213	BR 213	BR 213	BR 218
V	36	8	244	234	220	218
Cr	4	17	62	56	65	148
Rb	154	210	103	116	98	15
Sr	274	63	397	455	472	861
Y	6.7	4.0	20	21	17	57
Zr	127	47	249	289	223	453
Nb	44	17	58	69	52	241
Cs	2.04	0.99	1.19	1.02	0.65	0.22
Ba	255	116	562	636	515	685
La	26	8.6	30.0	33.7	26.4	54.3
Ce	41	14.2	57.6	66.5	52.7	130.8
Nd	14	4.7	25.9	29.2	23.1	83.0
Sm	2.24	0.52	4.5	5.0	4.3	16.7
Eu	0.32	0.00	1.15	1.41	0.96	4.0
Gd	1.79	0.56	4.5	4.7	4.2	15.5
Dy	1.29	0.73	3.8	4.3	3.2	11.8
Er	0.73	0.45	2.00	1.81	1.63	5.3
Yb	0.69	0.49	2.18	2.09	1.72	5.1

Table 7 Oxygen isotopic composition of minerals from Greene Point and Baker Rocks spinel peridotites and standard deviation of the mean (SEM)

Sample	δ^{18}O Opx (‰ SMOW)	SEM	δ^{18}O Ol (‰ SMOW)	SEM	δ^{18}O Cpx (‰ SMOW)	SEM	δ^{18}O Spl (‰ SMOW)	SEM
GP5	5.90	0.10	5.47	0.07	5.32	0.13		
GP6	5.72	0.03	5.12	0.13	4.96	0.19		
GP10	5.79	0.04	5.30	0.09	5.37	0.02	3.19	0.11
GP14	5.70	0.09	5.55	0.04	5.62	0.07		
GP22	5.77	0.08	5.39	0.10	4.99	0.12		
GP25	6.04	0.12	5.25	0.07	5.13	0.15		
GP28	5.61	0.03	5.09	0.03	5.24	0.13		
GP29	5.56	0.10	5.35	0.15	5.34	0.02		
GP31	6.00	0.06	5.36	0.13	5.15	0.04		
GP34	5.90	0.07	5.40	0.01	5.42	0.05		
GP36	5.89	0.01	5.42	0.02	5.26	0.06		
GP42	5.82	0.06	5.58	0.07	5.53	0.07	4.88	0.04
GP49	5.71	0.16	5.81	0.09	5.35	0.11		
BR213	6.00	0.18	4.80	0.08	5.10	0.13		
BR218	5.96	0.01	5.79	0.06	5.62	0.07	4.43	0.09
BR218[a]	6.14		5.67	0.05	5.71			
BR219	5.87	0.16	4.96	0.01	5.12	0.20	3.79	0.21

BR218 Amphibole $\delta^{18}O = 5.16‰$ and GP Lava Host (SAX20) $\delta^{18}O = 5.85‰$
[a]Minerals near to the amphibole vein in composite xenolith

further 3–15% of melting in the spinel stability field (Fig. 10b).

The not-metasomatized samples are characterized by significant linear covariations of $\delta^{18}O_{cpx}$ versus cpx modal abundance ($R^2 = 0.761$) and versus F ($R^2 = 0.948$; Fig. 11a, b), whereas poor correlations are defined by the $\delta^{18}O_{cpx}$ values of the metasomatized samples ($R^2 \leq 0.433$). The $\delta^{18}O_{spl}$ values define a noticeable covariation trend ($R^2 = 0.953$) with spl–Cr# (and therefore F, $R^2 = 0.999$; Fig. 11c), regardless of the metasomatic overprint. These relationships are consistent with the effects caused by partial melting. If partial melts derived from spl–lherzolite are more siliceous than the residual assemblage (Hirschmann et al. 1998), the ^{18}O-isotope fractionation in the more polymerized phase (e.g. Garlik 1966; Appora et al. 2003) is consistent with a decrease in $\delta^{18}O$ of cpx and depends on the extent of partial melting. In contrast, the $\delta^{18}O_{opx}$ and $\delta^{18}O_{ol}$ values show only slight variations likely resulting from the minor contribution of olivine and orthopyroxene to partial melting and their peritectic relationships. Moreover, the larger grain size of these phases in mantle xenoliths accounts for a difficult diffusion-assisted re-equilibration. Nevertheless, oxygen isotope disequilibrium fractionation has been documented for olivine and orthopyroxene in peridotites with no metasomatic (open-system) overprint, and this in spite of the large oxygen buffer of the mantle (e.g. Harmon et al. 1987; Deines and Haggerty 2000; Eiler 2001; Zhang et al. 2000).

If the $\delta^{18}O_{cpx}$ values are controlled by the liquid/solid partition coefficients at the melting temperature and vary as a function of T, we may assume a major cpx control on the isotopic composition of the melt. Using the approximation:

$$1000 \ln \alpha_{melt-cpx} = \delta^{18}O_{melt} - \delta^{18}O_{cpx} = \Delta^{18}O_{melt-cpx}$$

(e.g O'Neil 1986), simple mass balance considerations imply that melting processes is described by the equation:

$$\delta^{18}O_{cpx}^{initial} = F \times \delta^{18}O_{melt} + (1 - F) \times \delta^{18}O_{cpx}$$

(F is the fraction of partial melting derived from the no-modal fractional melting equation of Hellebrand et al. 2002).

After little manipulation:

$$\delta^{18}O_{cpx} = \delta^{18}O_{cpx}^{initial} - F\Delta_{melt-cpx}.$$

In principle, this equation could explain the linear dependence of $\delta^{18}O_{cpx}$ from F (Fig. 11b). The intercept and the slope of the linear array also provide estimates for the peridotite ^{18}O- starting composition and for the $\Delta^{18}O_{melt\text{-}cpx}$, respectively. The calculated $\delta^{18}O_{cpx}^{initial}$ approximates 5.68‰, in the range of peridotite cpx on world-wide scale (Mattey et al. 1994). In contrast, the $\Delta^{18}O_{melt\text{-}cpx}$ derived from the slope (~2.95) is inconsistent with equilibrium fractionation between peridotite residuum and partial melts ($\Delta_{melt\text{-}cpx} = 0.2$; Zhao and Zheng 2003) and ultimately unrealistic for ^{18}O-isotope fractionation at mantle conditions.

Rearrangement and differentiation of the above equation results into:

$$\frac{\partial(\delta^{18}O_{cpx}^{initial} - \delta^{18}O_{cpx})}{\partial F} = \Delta_{melt-cpx} = \frac{-\partial(\delta^{18}O_{cpx})}{\partial F}$$

In this equation, F is imposed by the mass balance and the $\Delta_{melt\text{-}cpx}$ values strongly depend on the rate of change in $\delta^{18}O_{cpx}$ with F. This condition is achieved only if the melt is subtracted from the matrix after its

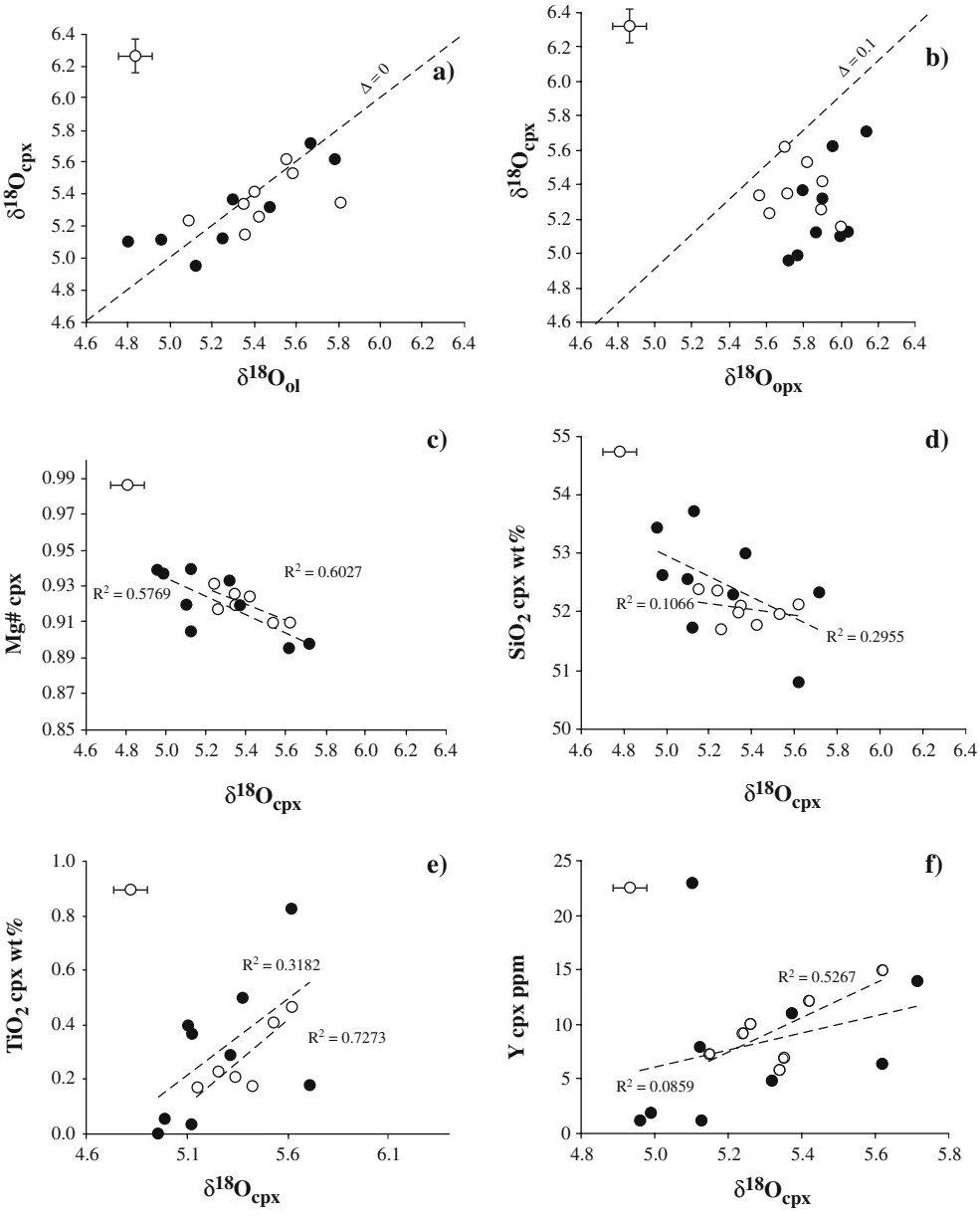

Fig. 9 Oxygen isotopic composition for olivine, orthopyroxene and clinopyroxene for NVL spinel peridotites. The line in (**a**) and (**b**) corresponds to $\Delta^{18}O = 0$. *Open circle* represents not metasomatized sample; *filled symbols* represent metasomatized sample. **c** and **d** plots show the negative correlation of Mg# and SiO_2 content with the $\delta^{18}O_{cpx}$ values. On the contrary the $\delta^{18}O_{cpx}$ is positively correlated with TiO_2 and Y contents, (**e**) and (**f**) respectively

formation, thereby implying that the dependence of $\delta^{18}O_{cpx}$ from F may be described only by a fractional melting model. Present data indicate that the correlations among the $\delta^{18}O_{cpx}$ and the parameters related to the extent of fractional melting hold in the not-metasomatized samples; the $\delta^{18}O_{spl}$ versus Cr_{spl}# suggest that these correlations may also survive in samples which experienced low degrees (cryptic) of mantle metasomatism.

Mantle metasomatism

First order evidence for metasomatic events are represented by the high FeO, TiO_2 and incompatible trace element contents of the whole rock and pyroxenes. REE_N clinopyroxene patterns can be interpreted in terms of a chromatographic fractionation during reactive porous flow (Navon and Stolper 1987; Bodinier et al. 1990; Bedini et al. 1997; Vernières et al. 1997). In the chromatographic model, the behaviour of elements during melt percolation through the peridotite depends on mineral-melt partition coefficient ($D^{rock/melt}$). The interaction of the percolating melt with the peridotite assemblage causes the melt to be progressively enriched in LREE, producing a transient metasomatic zoning with different enrichment patterns as a function of the distance from the magma source (Ionov et al. 2002). Metasomatism can be referred to as "wall-rock" metasomatism, linked to the transport of melt in fractures (veins and dykes), and "diffuse" metasomatism related to percolation of small melt fractions along grain boundaries in the peridotite matrix. Peridotites (and cpx) affected by "wall-rock" metasomatism are generally characterized by Fe-enrichment and convex-upward or

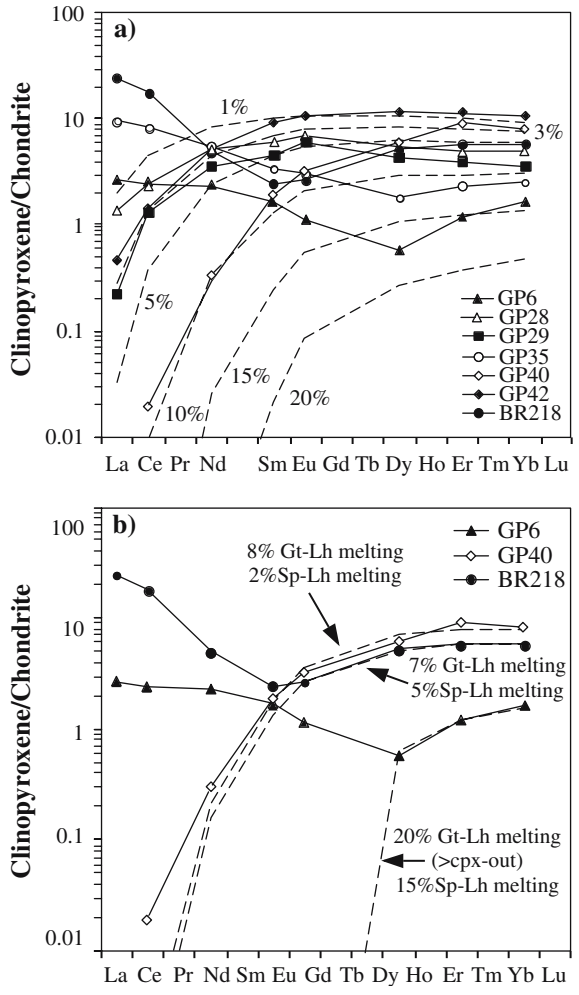

Fig. 10 REE chondrite normalised patterns of NVL clinopyroxene compared with the results of fractional melting model (Johnson et al. 1990) in the spinel stability field (**a**) and a combination of initial melting in the garnet stability field followed by additional melting in the spinel stability field (**b**). Initial source composition, sources modes, melt modes and distribution coefficients are after Hellebrand et al. (2002). Chondrite normalization values taken from McDonough and Sun (1995)

flat REE patterns, whereas Fe-enrichment are absent and the REE patterns are highly fractionated (from U-shaped to steadly enriched patterns) where "diffuse" metasomatism has been active (Bodinier et al. 1990; Bedini et al. 1997; Ionov et al. 2002, Xu and Bodinier 2004).

Composite sample BR218 is typical in this respect: the clinopyroxene next to the veins are FeO-enriched, with convex-upward REE patterns; far (~5 cm) from the vein, cpx REE pattern becomes convex-downward. This can be interpreted as a shift from "wall-rock" to "diffusive" metasomatism linked to different melt/rock ratios, as required in the chromatographic fractionation (Kelemen et al. 1995; Bedini et al. 1997; Xu and Bodinier 2004).

Textural relations, FeO enrichments and the REE pattern of BR218*clinopyroxene, indicate that its composition approached equilibrium with the metasomatic melt. Using crystal/melt partition coefficients (Skulski et al. 1994; Halliday et al. 1995) and trace element composition of BR218* cpx, it is possible to estimate the trace element concentrations of the melt in

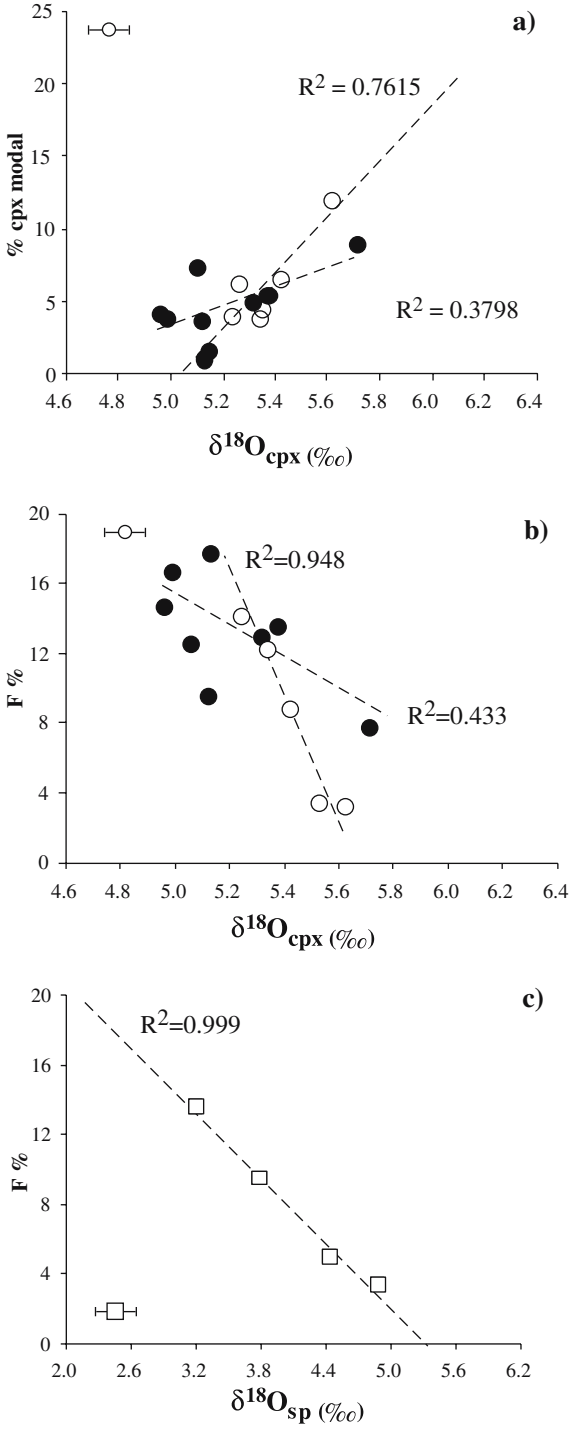

Fig. 11 (**a**) Variation of oxygen isotope composition of clinopyroxene with its modal abundance in NVL spinel peridotites. The $\delta^{18}O$ values of clinopyroxene (**b**) and spinel (**c**) decrease with the degree of partial melting suggesting that partial melting have a primary control on the oxygen isotope composition of clinopyroxene

equilibrium with this cpx. The calculated liquid shows trace element pattern similar to that of the GP host lava (SAX20, Tab. 5), although with lower Nb and Ta contents, and more negative Ti anomaly (Fig. 12). The differences between calculated liquid and host GP lava can be due to the crystallization of amphibole in the vein, that likely depleted the residual melt in Nb, Ta and Ti. This melt percolated away from the vein and interacted with the peridotite assemblage producing a cpx (sample BR218) with negative Nb, Zr and Hf anomalies, fractionated LREE patterns and decoupled Nb–Ta contents (Ionov et al. 2002; Xu and Bodinier 2004). Similarly, a process of diffusive metasomatism might be responsible for variable incompatible elements enrichments of GP samples. These samples probably represent peridotite portions at various distance from the melt conduit (vein and/or dyke). From the composition of calculate equilibrium melts (GP10 and BR218*), the metasomatic agents for BR and GP xenoliths is inferred to be similar in composition to the nephelinite GP host lava, although the high ascent rates and the resulting short scale diffusion-controlled effects prevent the host lavas itself to be the very metasomatic agent.

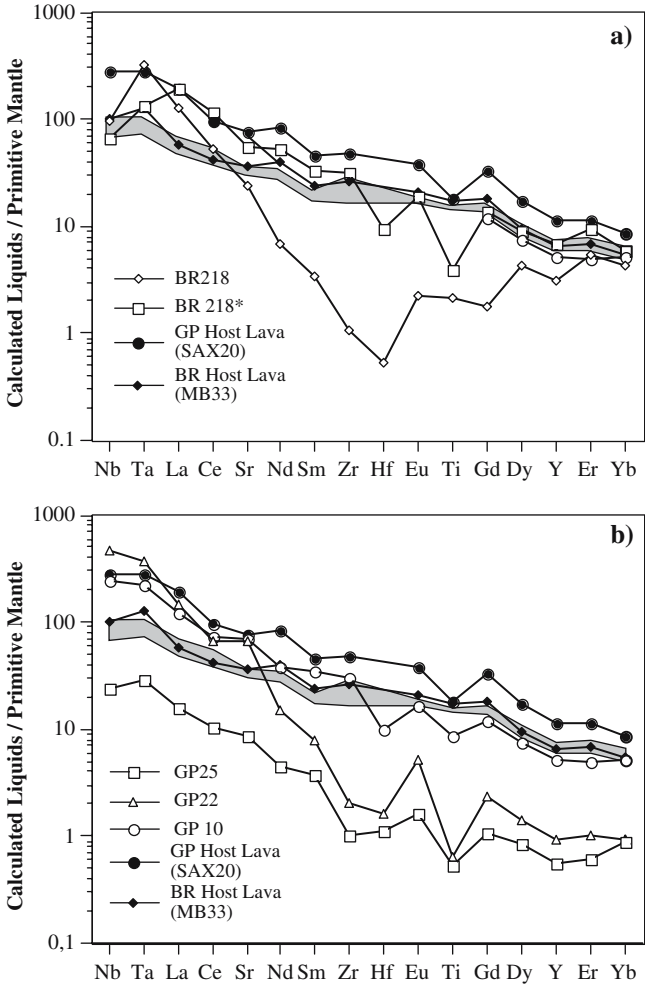

Fig. 12 PM normalized incompatible patterns of calculated liquid in equilibrium with enriched clinopyroxene of xenoliths. The calculations are made using cpx/liquid distribution coefficient proposed by Skulski et al. (1994) and Halliday et al. (1995). The figure also reports the range of variation of some incompatible elements (*grey field*) of basic McMurdo Lavas (Rocchi et al. 2002)

The metasomatic events were able to shift the $\delta^{18}O_{cpx}$ values only where the (metasomatic) fluid/rock ratio was high, as likely in the case of sample BR218* (vein).

Assuming (1) the $\delta^{18}O$ of the metasomatic agent to be similar to the $\delta^{18}O$ value of nephelinite sample SAX20 ($\delta^{18}O_{WR} = 5.85‰$); (2) the $\delta^{18}O_{cpx}^{initial} = 5.60$ (Mattey et al. 1994); and (3) using a $\Delta^{18}O_{cpx\text{-}Met}$ values ($\Delta^{18}O_{cpx\text{-}Met}$ = fractionation between the peridotite cpx and the metasomatic melt) of 0.15‰ at 1100°C (Zhao and Zheng, 2003), it is possible to calculate the variation of the $\delta^{18}O_{cpx}$ value as a function of the mass ratio between the rock (P) and the metasomatic melt ($\frac{P}{Met}$) by the simple mass balance calculation:

$$\frac{P}{Met} = \frac{(\delta^{18}O_{cpx}^{final} - \delta^{18}O_{cpx}^{initial})}{\delta^{18}O_{Met}^{initial} - (\delta^{18}O_{cpx}^{final} - \Delta_{cpx-Met})}$$

On these bases, a maximum $\frac{P}{Met}$ ratio of 0.38 would be required to shift the $\delta^{18}O_{cpx}$ values of sample BR218 to 5.71‰. This value is plausible and consistent with textural relationships between vein and peridotite in composite sample BR218.

Diffusion-based calculation (Crank 1975) provides time estimates for zoning to be achieved in crystals with core-rim REE variations (Fig.5; Table 4). The equation $x = (Dt)^{-2}$ approximates the time required for an element to travel the distance x in a time "t". For diffusion coefficients $D_{REE} \approx 10^{-21}$ m^2/s (Van Orman et al. 2001), larger crystals (Ø = 2 mm) would be completely homogenized in a time span between 10 and 40 millions of years. In a similar time interval, oxygen isotope disequilibrium may survive among coarse-grained minerals at mantle conditions (e.g. Ryerson et al. 1989; Ingrin et al. 2001

Origin of intergranular glass patches

Late evidence of melting is also provided by the occurrence of alkaline glasses in the spongy rims of clinopyroxenes and by interstitial blebs of alkaline glass in reaction with spinel ± clinopyroxene. Both these textural features result from xenolith disequilibrium melting during the transport into the host lava, due to rapid P–T variations (Francis 1976; Dawson 2002). The high glass concentrations of K, P, Rb and Ba indicate that amphibole and/or phlogopite were probably involved into the melting reactions (e.g. Hornig and Wörner 1991; Beccaluva et al. 1991; Coltorti et al. 2004); the absence of these hydrous phases in Greene Point xenoliths is likely due to their complete exhaustion during melting.

Sub-alkaline glasses found in sample BR213 were produced from the reaction between SiO_2-poor melt and the depleted peridotite, this reaction produces a distinctive Si–Al-rich hybrid melt (Zinngrebe and Foley

1995; Shaw and Edgar 1997). Similar glasses, although showing lower Al_2O_3 contents, have been experimentally produced by orthopyroxene/basanite interaction (Shaw 1999). Higher Al_2O_3 contents in glasses of NVL xenoliths, and high Cr_2O_3 contents of associated Cpx II, likely account for the contribution of spinel to the glass-forming reaction.

Though somehow related to trace element patterns of McMurdo Volcanic Group, subalkaline and alkaline glass compositions do not match those of mafic lavas of MMVG, confirming that they are the product of dis-equilibrium reactions.

Thermal regime

Thermometric (two-pyroxene geothermometer; Wells 1977; Brey and Köhler 1990) and barometric estimates (olivine–clinopyroxene Ca-exchange reaction; Köhler and Brey 1990) show that coarse crystals of xenoliths were equilibrated in the spinel peridotite field (Table 8; Fig. 13) at T between $950 < T < 1050$°C and P between $1.0 < P < 1.5$ GPa. The P–T data of primary phases of the peridotite assemblage (squares) are close to the hydrous peridotite solidus ($H_2O < 0.4$wt%; Falloon et al. 1988; Falloon et al. 1999).

Estimates of equilibrium T and P obtained on the crystal cores were compared with data from Mt. Melbourne xenoliths (Beccaluva et al. 1991) and with the data defined by geotherms typical of stationary and dynamic rifts (Chapman 1986).

The higher temperature array of our data defines a geotherm of about 80°C/GPa at $P > 1$ GPa, compatible with a dynamic rift geotherm. This implies a larger heat supply than previously thought on the basis of a 40°C/GPa geotherm (Berg et al. 1989). This new geotherm meets the hydrous solidus of peridotite at about 2 GPa, running close to the hydrous peridotite solidus. This suggests that low degree partial melts had the possibility to migrate through the peridotite matrix.

In near-primary melts erupted in NVL, the estimated conditions for olivine crystallization are in the range of 1250–1350°C at pressures between 2.0 and 2.5 GPa (Orlando et al. 1997). These conditions likely correspond to the mantle potential temperature (Tp; Green et al. 2001); they also match the common Tp values of the asthenosphere and its thermal boundary layer (Anderson 1995; McKenzie and Bickle 1988). Starting from these P–T conditions and assuming an adiabatic coefficient of 30°C/GPa, the estimated mantle geotherm sets the conditions for the genesis of McMurdo melts at $4 \le P \le 5$ GPa (corresponding to depths greater than 120 km) and $1350 \le T \le 1400$°C. These mantle potential

Table 8 Temperature and pressure estimes for peridotites from Greene Point and Baker Rocks

	T (°C), Wells (1977)	T (°C), Köhler and Brey, (1990)	P (GPa), Köhler and Brey (1990)
BR213	1027	1041	1.1
BR218	981	981	0.9
BR219	1061	1047	1.2
GP 1	970	948	1.0
GP 5	959	940	
GP 6	1043	1035	1.2
GP 10	1004	1016	1.4
GP 14	998	1033	1.4
GP 15			
GP 17	936	1039	1.1
GP 20	1045	1019	1.4
GP 21			
GP 22	1062	1062	1.4
GP 25			
GP 28	944	944	1.4
GP 29	941	941	1.5
GP 34	1007	959	1.4
GP 36	1028	1031	1.0
GP 49	925	925	0.9

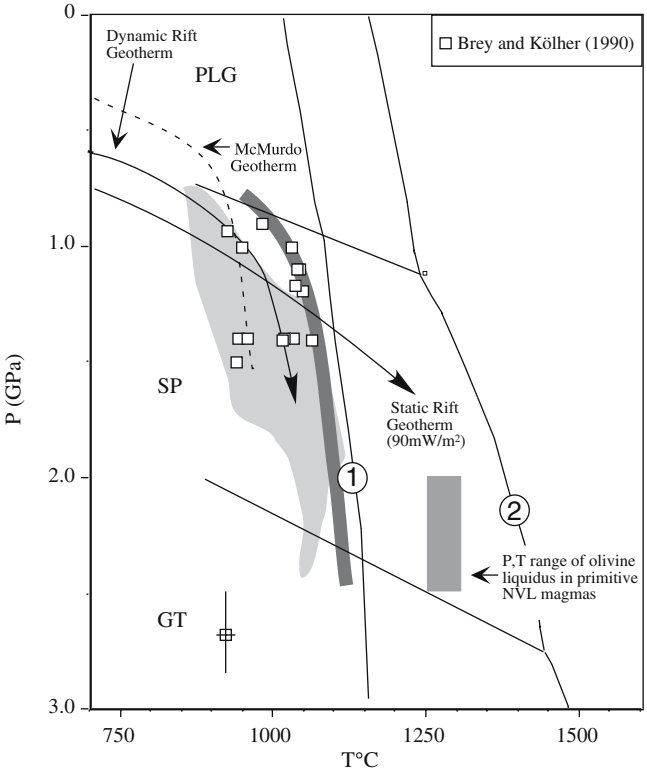

Fig. 13 Temperature (°C) and pressure (GPa) estimates from North Victoria Land mantle xenoliths. *Squares* represent two pyroxene thermometer (Brey and Kölher 1990) combined to barometer Ol-Cpx (Kölher and Brey 1990). *Error bars* are reported in the figure. McMurdo geotherm from Berg et al. (1989). Static and dynamic rift geotherms are from Chapman (1986). PLG, SP and GT:PT ranges of stability of plagioclase, spinel and garnet. Curves 1 and 2 are the hydrous (0.4 wt% H_2O) and anhydrous peridotite solidi (Falloon et al. 1988; Falloon et al. 1997; Green 1988). *Light grey field* represents the PT range of mantle xenoliths from NVL reported in (Beccaluva et al. 1991). *Gray rectangle* represents the PT range for the onset of olivine crystallization in near primary melts of NVL (Orlando et al. 1997). *Heavy grey line* represents the NVL mantle geotherm visually fitted from the high temperature envelop of our PT determinations: $P > 1$ Gpa, the gradient is 80°C/GPa. See text for discussion

temperatures are at least 200–300°C lower than estimates expected for a thermally buoyant plume (Shubert et al. 2001). Thus decompressional melting of fertile or re-enriched lithospheric mantle (Orlando et al. 2000; Rocchi et al. 2002) in a regime of transtensional tectonics (Salvini et al. 1997) turns out to be a more satisfactory explanation for the genesis of magma in NVL.

The frame emerging from trace elements and oxygen isotopic data is in agreement with the conclusions derived by Zipfel and Wörner (1992), reconstructing the thermal history of NVL lithospheric mantle. These authors, on the basis of diffusion profile of Ca in the mantle olivines, stated that the thermal state of the lithospheric during Cenozoic evolved from normal temperature gradient to a dynamic rift geotherm as a consequence of the onset of magmatic activity.

Conclusions

The chemical and isotopic data on mantle xenoliths from northern Victoria Land constrain the compositional evolution of the mantle underneath the Ross Sea region of Antarctica. Extraction of silicate melt via different degrees of partial melting affected the spinel-peridotite mantle. Partial melting was followed by cryptic and modal metasomatic events, resulting in chemical and mineralogical heterogeneities of the peridotite. These metasomatic effects are characterized by Fe–Ti addition and variable LREE enrichments of the clinopyroxene. The occurrence of veins of fertile wehrlite or hornblendite is related to the infiltration of magmas at mantle depths. In addition, disequilibrium melting/reactions during the ascent to surface produced intergranular high Mg# and Si-rich melts.

The $\delta^{18}O$ values indicate non-equilibrium oxygen isotope fractionation at mantle depths and the $\delta^{18}O_{cpx}$ and $\delta^{18}O_{spl}$ correlations with F are consistent with a process of fractional melting. Metasomatic overprint affected the $^{18}O/^{16}O$ ratios of the minerals only where the metasomatic-melt/rock ratios were high and likely occurred no more than 40 Ma bp.

Thermobarometric estimates reveal a progressive heating of the mantle in a thermal regime of dynamic rifting. A geotherm of 80°C/GPa is proposed for the conductive refractory lithosphere of NVL close to the hydrous solidus of peridotite. The mantle potential temperature for the origin of near primary melts crosses the geotherm at 1350–1400°C and 4–5 GPa (120–150 km). This thermal regime is coherent with the hypothesis of decompressional melting induced by transtensive tectonic regime and conflicts with the presence of an active plume in the area of the Ross Sea.

Acknowledgements This Work has been funded by CNR-PNRA project, grants PEA 1999/2000. An earlier version of the manuscript benefited from the constructive review of D.H. Green. Constructive reviews of C.G Macpherson and an anonymous reviewer are highly appreciated.

References

Anderson DL (1995) Lithosphere, asthenosphere, and perisphere. Rev Geophys 33:125–149

Appora I, Eiler J, Matthews A, Stolper EM (2003) Experimental determination of oxygen isotope fractionations between CO_2 vapor and sodamelilite melt. Geochim Cosmochim Acta 67:459–471

Armienti P, Tarquini S (2002) Power-law olivine crystal size distributions in lithospheric mantle xenoliths. Lithos 65:273–285

Asprey LB (1976) The preparation of very pure F_2 gas. J Fluor Chem 7:359–361

Beccaluva L, Coltorti M, Orsi G, Saccani E, Siena F (1991) Nature and evolution of subcontinental lithospheric mantle of Antarctica: evidence from ultramafic xenoliths of the Melbourne volcanic province (northern Victoria Land, Antarctica). Mem Soc Geol It 46:353–370

Bedini RM, Bodinier J-L, Dautria J-M, Morten L (1997) Evolution of LILE-enriched small melt fractions in the lithospheric mantle: a case study from the East African Rift. Earth Planet Sci Lett 153:67–83

Behrendt JC, LeMausurier W, Cooper AK, Tessensohn F, Tréhu A, Damaske D (1991) Geophysical studies of the West Antarctic Rift System. Tectonics 10(6):1257–1273

Behrendt JC, LeMausurier W, Cooper AK (1992) The West Antarctic Rift System—a propagating rift captured by a mantle plume? Recent progress in Antarctic Earth science. Yashida Y et al.(ed): pp 315–322

Berg JH, Moscasti RJ, Herz DL (1989) A petrologic geotherm from a continental rift in Antarctica. Earth Planet Sci Lett 93:98–108

Bodinier JL, Vasseur G, Vernieres J, Dupuy C, Fabries J (1990) Mechanism of mantle metasomatism geochemical evidence from the Lherz orogenic peridotite. J Petrol 31:597–628

Bottazzi P, Ottolini L, Vannucci R, Zanetti A (1994) An accurate procedure for the quantification or rare earth elements in silicates. In: Benninghoven A et al. (ed) Secondary ion mass spectrometry - SIMS IX. Wiley, Chichester, pp 927–930

Brey GP, Köhler TP (1990) Geothermometry in four-phase Lherzolites II: new thermobarometers and practical assessment of existing thermobarometers. J Petrol 31:1353–1378

Chand S, Radhakrishna M, Subrahmanyam C (2001) India-East Antarctica conjugate margins: rift-shear tectonic setting inferred from gravity and bathymetry data. Earth Planet Sci Lett 185:225–236

Chapman DS (1986) Thermal gradients in continental crust. In: DAC Dawson JB, Hall J, Weedepohl KH:"The nature of the lower continental crust". Geol Soc London Spec Publ: pp 63–70

Chazot G, Lowry D, Menzies M (1997) Oxygen isotopic composition of hydrous and anhydrous mantle peridotites. Geochim Cosmochim Acta 61:161–169

Clayton RN, Mayeda TK (1983) Oxygen isotopes in eucrites, shergottites, nakhilites, and chassignites. Earth Planet Sci Lett 62:1–6

Coltorti M, Beccaluva L, Bonadiman C, Faccini B, Ntaflos T, Siena F (2004) Amphibole genesis via metasomatic reaction with clinopyroxene in mantle xenoliths from Victoria Land, Antarctica. Lithos 75:115–139

Crank J (1975) The mathematics of diffusion. Clarendon, Oxford

Dawson JB (1984) Contrasting types of upper-mantle metasomatism. In: Kornprobst J (ed) Kimberlits II. The mantle and crust-mantle relationships. Elsevier, Amsterdam, pp 289–294

Dawson JB (2002) Mestasomatism and partial melting in Upper-Mantle Peridotite xenoliths from the Lashaine Volcano, Northern Tanzania. J Petrol 43:1749–1777

Deines P, Haggerty SE (2000) Small-scale oxygen isotope variations and petrochemistry of ultradeep (> 300 km) and transition zone xenoliths. Geochim Cosmochim Acta 64:117–131

Eiler JM (2001) Oxygen isotope variation in basaltic lavas and upper mantle rocks. In Valley JW, Cole DR (eds) Stable isotope geochemistry. Rev Mineral Geochem 43:319–364

Falloon TJ, Green DH, Hatton CJ, Harris KR (1988) Anhydrous partial melting of a fertile and depleted peridotite from 2 to 30 kb and application to basalt petrogenesis. J Petrol 29:1257–1287

Falloon TJ, Green DH, O'Neill HSTC, Hibberson WO (1997) Experimental tests of low degree peridotite partial melt compositions: implications for the nature of anhydrous near-solidus peridotite melts at 1 GPa. Earth Planet Sci Lett 152:149–162

Falloon TJ, Green DH, Danyushevsky LV, Faul UH (1999) Peridotite melting at 1.0 and 1.5 GPa: an experimental evaluation of techniques using diamond aggregates and mineral mixes for determination of near-solidus melts. J Petrol 40:1343–1375

Fitzgerald PG (1994) Thermochronologic constraints on post-paleozoic tectonic evolution of the central Transantarctic Mountains. Antarctica Tectonics 132:878–836

Fitzgerald PG, Stump E (1997) Cretaceous and Cenozoic episodic denudation of the Transantarctic Mountains, Antarctica: new constraints from apatite fission track thermochronology in the Scott Glacier region. J Geophys Res 102(B4):7747–7765

Francis DM (1976) The origin of amphibole in lherzolite xenoliths from Nunivac Island, Alaska. J Petrol 17:357–378

Franzini M, Leoni L, Saitta M (1975) Revisione di una metodologia analitica per fluorescenza-X, basata sulla correzione completa degli effetti di matrice. Rend Soc It Min Petr 31:365–378

Frey FA, Green DH (1974) The mineralogy, geochemistry and origin of lherzolite inclusions in Victoria basanites. Geochim Cosmochim Acta 38:1023–1059

Frey FA, Suen CJ, Stockman HW (1985) The Ronda high temperature peridotite: geochemistry and petrogenesis. Geochim Cosmochim Acta 49:2469–2491

Gamble JA, McGibbon F, Kyle PR, Menzies MA, Kirsch I (1988) Metasomatised xenoliths from Foster Crater, Antarctica: implications for lithospheric structure and processes beneath the Transantarctic Mountain front. J Petrol Special Lithosphere Issue:109–138

Garlik GD (1966) Oxygen isotope fractionation in igneous rocks. Earth Planet Sci Lett 1:361–368

Green DH (1973) Experimental melting studies on a model upper mantle composition at high pressure under water-saturated and water-undersaturated conditions. Earth Planet Sci Lett 19:37–53

Green DH, Falloon T, Eggins S, Yaxley G (2001) Primary magmas and mantle temperatures. Eur J Mineral 13:437–451

Gregory RT, Taylor HP (1986a) Possible non-equilibrium oxygen isotope effects in mantle nodules, an alternative to the Kyser-O'Neil-Carmichael $^{18}O/^{16}O$ geothermometer. Contrib Mineral Petrol 93:114–119

Gregory RT, Taylor HP (1986b) Non equilibrium, metasomatic $^{18}O/^{16}O$ effects in upper mantle mineral assemblages. Contrib Mineral Petrol 93:124–135

Halliday AN, Lee DC, Tommasini S, Davies GR, Paslick CR (1995) Incompatible trace elements in OIB and MORB and source enrichment in the sub-oceanic mantle. Earth Planet Sci Lett 133:379–395

Harmon RS, Kempton PD, Stosch HG, Hoefs J, Kovalenko VI, Eonov-D (1987) $^{18}O/^{16}O$ ratios in anhydrous spinel lherzolite xenoliths from the Shavaryn-Tsaram Volcano, Mongolia. Earth Planet Sci Lett 81(2–3):193–202

Hart SR, Blusztajn J, LeMasurier E, Rex DC (1997) Hobbs Coast Cenozoic volcamism: implications for the Weat Antarctic rift system. Chem Geol 139:223–248

Hellebrand E, Snow JE, Dick HJB, Hofmann AW (2001) Coupled major and trace elements as indicators of the extent of melting in mid-ocean-ridge peridotites. Nature 410:677–681

Hellebrand E, Snow JE, Hoppe P, Hofmann AW (2002) Garnet-field melting and late-stage refertilization in ''residual'' abyssal peridotites from the Central Indian Ridge. J Petrol 43:2305–2338

Hirschmann MM, Ghiorso MS, Wasylenki LE, Asimov PD, Stolper EM (1998) Calculation of peridotite partial melting from thermodynamic models of minerals and melts. I. Review of methods and comparison with experiments. J Petrol 39:1091–1115

Hornig I, Wörner G (1991) Zirconolite-bearing ultra-potassic veins in a mantle xenolith from Mt. Melbourne Volcanic field (Victoria Land, Antarctica). Contrib Mineral Petrol 106:355–366

Hornig I, Wörner G, Zipfel J (1992) Lower crustal and mantle xenoliths from Mt. Melbourne Volcanic field, Northern Victoria Land, Antarctica. Mem Soc Geol It 46:337–352

Ingrin J, Pacaud L, Jaoul O (2001) Anisotropy of oxygen diffusion in diopside. Earth Planet Sci Lett 192:347–361

Ionov DA, Bodinier JL, Mukasa SB, Zanetti A (2002) Mechanisms and sources of mantle metasomatism: major and trace element composition of peridotite xenoliths from Spitsbergen in the context of numerical modelling. J Petrol 43:2219–2259

Irvine TN, Baragar WRA (1971) A guide to the chemical classification of the common volcanic rocks. Can J Earth Sci 8:523–548

Irving AJ, Frey FA (1984) Trace element abundances in megacrysts and their host basalts: constrains on partition coefficients and megacrysts genesis. Geochim Cosmochim Acta 48:1201–1221

Johnson KTM, Dick HJB, Shimizu N (1990) Melting in the oceanic upper mantle: an ion microprobe study of diopside in abyssal peridotites. J Geophys Res 95:2661–2678

Kelemen PB, Whitehead JA, Aharonov E, Jordahl KA (1995) Experiments on flow focusing in soluble porous media, with application to melt extraction from the mantle. J Geophys Res 100:475–496

Köhler TP, Brey GP (1990) Calcium exchange between olivine and clinopyroxene calibrated as a geothermobarometer for natural peridotites from 2 to 60 kb with calibrations. Geochim Cosmochim Acta 54:2375–2388

Kyle PR (1990) McMurdo volcanic group-western Ross Embayment: introduction. In: LeMasurier WE, Thomson JW (eds) Volcanoes of the Antarctic plate and southern oceans. Am Geophys Union Washington DC, pp 19–25

Kyle PR, McIntosh WC, Panter K, Smellie J (1992) Is volcanism in Marie Byrd Land related to a mantle plume? In: Yoshida Y, Kaminuma K, Shiraishi K (eds) Recent progress in Antarctic earth science. TERRAPUB, Tokyo, p 337

Kyser T K, O'Neil JR, Carmichael ISE (1981) Oxygen isotope thermometry of basic lavas and mantle nodules. Contrib Mineral Petrol 77:11–23

Le Bas MJ, Le Maitre RW, Streckeisen A, Zanettin R (1986) A chemical classification of volcanic rocks based on total alkali-silica diagram. J Petrol 27:745–750

LeMasurier WE, Landis CA (1996) Mantle plume activity recorded by low relief erosion surfaces in West Antarctica and New Zealand. Geol Soc Am Bull 108:1450–1466

LeMasurier WE, Rex DC (1989) Evolution of linear volcanic ranges in Marie Byrd Land, West Antarctica. J Geophys Res 94:7223–7236

LeMasurier WE, Thomson JW (1990) Volcanoes of the Antarctic plate and southern oceans. Antarctic research series, 18 Washington, DC American Geophysical Union: pp 487

Macpherson C, Mattey D (1998) Oxygen isotope variations in Lau Basin Lavas. Chem Geol 144:177–194

Mattey D, Lowry D, Macpherson C (1994) Oxygen isotope composition of mantle peridotite. Earth Planet Sci Lett 128:231–241

McDonough WF, Sun S-s (1995) The composition of the earth. Chem Geol 120:223–253

McKenzie D, Bickle MJ (1988) The volume and composition of melt generated by extension of the lithosphere. J Petrol 29:625–679

Muller P, Schmidt-Tomè M, Kreuzer H, Thessensohn F, Vetter U (1991) Cenozoic peralkaline magmatism at the western Margin of the Ross Sea, Antarctica. Proceedings of the meeting ''Earth Science investigations in Antarctica'' Siena, 4–6 October 1989 - Mem Soc Geol It XLVI, pp. 315–336

Navon O, Stolper E (1987) Geochemical consequence of melt percolation: the upper mantle as chromatographic column. J Geol 95:285–307

Nickel KG, Green DH (1984) The nature of upper-most mantle beneath Victoria Australia as deduced from ultramafic xenolith. Kimberlite II: the mantle and crust-mantle relationships. Proceeding of the 3rd international Kimberlite conference. Amsterdam, Elsevier pp. 161–178

Niu Y (1997) Mantle melting and melt extraction processes beneath ocean ridges: evidence from Abyssal peridotites. J Petrol 38: 1047–1074

Norman MD (1998) Melting and metasomatism in the continental lithosphere: laser ablation ICPMS analysis of minerals in spinel lherzolites from eastern Australia. Contrib Mineral Petrol 130:240–255

O'Neil JR (1986) Terminology and standards. In: Valley JW, Taylor HP Jr, O'Neil JR, editors. Stable isotopes in high temperature geological processes. Reviews in mineralogy. Chelsea: Mineralogical Society of America; 1986. pp 561–570

Orlando A, Armienti P, Conticelli S, Vaggelli G, Manetti P (1997) Petrologic investigations on the primitive Cainozoic lavas of Northern Victoria Land, Antarctica. VII ISAES. The Antarctic region, geological evolution and processes, pp 523–530

Orlando A, Conticelli S, Borrini D, Armienti P (2000) Experimental study on a primary basanite from McMurdo volcanic group, Antarctica: inference on its mantle source. Antarctic Sci 12/1:105–116

Perinelli C, Armienti P, Trigila R, Aurisicchio C (1998) Intergranular melt inclusions within ultramafic xenoliths from Baker Rocks and Greene point volcanics (northern Victoria land, Antarctica. Terra Antarctica 5:217–233

Rocchi S, Armienti P, D'Orazio M, Tonarini S, Wijbrans J, Vincenzo GD (2002) Cenozoic magmatism in the western Ross Embayment: role of mantle plume vs. plate dynamics in the development of the West Antarctic rift system. J Geophys Res 107 B7:10.1029/(2001)

Rocholl A, Stein M, Molzahn M, Hart SR, Wörner G (1995) Geochemical evolution of rift magmas by progressive tapping of a stratified mantle source beneath the Ross Sea Rift, Northern Victoria Land, Antarctica. Earth Planet Sci Lett 131:207–224

Ryerson FJ, Durham WB, Cherniak DJ, Landford WA (1989) Oxygen diffusion in olivine: effect of oxygen fugacity and implication for creep. J Geophys Res 94:4105–4118

Salvini F, Brancolini G, Busetti M, Storti F, Mazzarini F, Coren F (1997) Cenozoic geodynamics of the Ross Sea region of Antarctica: crustal extension, intraplate strike-slip faulting and tectonic inheritance. J Geophys Res 102:24669–24696

Schubert G, Turcotte DL, Olson P (2001) Mantle convection in earth and planets. Cambridge University Press, Cambridge

Sharp ZD (1995) Oxygen isotope geochemistry of the Al_2SiO_5 polymorphs. Am J Sci 295:1058–1076

Shaw CSJ (1999) Dissolution of orthopyroxene in basanitic magma between 0.4 and 2 GPa: further implications for the origin of Si-rich alkaline glass inclusions in mantle xenoliths. Contrib Mineral Petrol 135:114–132

Shaw CSJ, Edgar AD (1997) Post-entrainment mineral-melt reactions in spinel peridotite xenoliths from Inver, Donegal, Ireland. Geol Mag 134:771–779

Skulsky T, Minarik W, Watson EB (1994) High pressure experimental trace-element portioning between clinopyroxene and basaltic melts. Chem Geol 117:127–147

Stagg HMJ, Willcox JB (1992) A case for Australia-Antarctica separation in the Neocomian (ca. 125 Ma). Tectonophysics 210:21–32

Storti F, Rossetti F, Salvini F (2001) Structural architecture and displacement accommodation mechanisms at the termination of the Priestly fault, northern Victoria Land, Antarctica. Tectonophysics 341:141–161

Takazawa E, Frey FA, Shimizu N (2000) Whole rock compositional variations in an upper mantle peridotite (Horoman, Hokkaido, Japan): are they consistent with a partial melting process? Geochim Cosmochim Acta 64:695–716

Taylor JHP, Epstein S (1962) Relationship between $^{18}O/^{16}O$ ratios in coexisting minerals of igneous and metamorphic rocks Part 2. Application to petrologic problems. Geol Soc Am Bull 73:675–694

Tessensohn F, Wörner G (1991) The Ross sea rift system (Antarctica): structure, evolution and analogues. In: Thomson MRA, Crame JA, Thomson JW (eds) Geological evolution of Antarctica. Cambridge University Press, Cambridge, pp 273–277

Tonarini S, Rocchi S, Armienti P, Innocenti F (1997) Constraints on timing of Ross Sea rifting inferred from Cainozoic intrusions from Northern Victoria Land, Antarctica. VII ISAES. The Antarctic region, geological evolution and processes, pp 511–522

Van Orman J, Grove TL, Shimizu N (2001) Rare earth element diffusion in diopside:influence of temperature, pressure, and ionic radius, and an elastic model for diffusion in silicates. Contrib Mineral Petrol 141:687–703

Vernières J, Godard M, Bodinier JL (1997) A plate model for the simulation of trace element fractionation during partial melting and magma transport in the earth's upper mantle. J Geophys Res 102:24771–24784

Wells PRA (1977) Pyroxene thermometry in simple and complex systems. Contrib Mineral Petrol 62:129–139

Wörner G (1999) Lithospheric dynamics and mantle sources of alkaline magmatism of the Cenozoic West Antarctic Rift System. Glob Planet Change 23:61–77

Wulff-Pedersen E, Neumann E-R, Vannucci R, Bottazzi P, Ottolini L (1999) Silicic melts produced by reaction between peridotite and infiltrating basaltic melts: ion probe data on glasses and minerals in veined xenoliths from La Palma, Canary Islands. Contrib Mineral Petrol 137:59–82

Xu YG, Bodinier JL (2004) Contrasting enrichments in high- and low-temperature mantle xenoliths from Nushan, Eastern China: results of a single metasomatic event during lithospheric accretion? J Petrol 45:321–341

Xu XS, O'Reilly SY, Griffin WL, Zhou XM (2000) Genesis of young lithospheric mantle in the southeastern China: a LAM-ICPMS trace element study. J Petrol 41:111–148

Zhang HF, Mattey DP, Grassineau N, Lowry D, Brownless M, Gurney JJ, Menzies MA (2000) Recent fluid processes in the Kaapvaal Craton, South Africa: Coupled oxygen isotope and trace element disequilibrium in polymict peridotites. Earth Planet Sci Lett 176:57–72

Zhao ZF, Zheng YF (2003) Calculation of oxygen isotope fractionation in magmatic rocks. Chem Geol 193:59–80

Zinngrebe E, Foley SF (1995) Metasomatism in mantle xenoliths from Gees, West Eifel, Germany: evidence for the genesis of calc-alkaline glasses and metasomatic Ca-enrichment. Contrib Mineral Petrol 122:79–96

Zipfel J, Wörner G (1992) Four- and five-phase peridotites from a continental rift system: evidence for upper mantle uplift and cooling at the Ross Sea margin (Antarctica). Contrib Mineral Petrol 111:24–36